Therapeutic inhibition of RBM20 improves diastolic function in a murine heart failure model and human engineered heart tissue

Radke M.H., Badillo-Lisakowski V., Britto-Borges T., Kubli D.A., Jüttner R., Parakkat P., Lopez Carballo J., Hüttemeister J., Liss M., Hansen A., Dieterich C., Mullick A.E., Gotthardt M.

This is the final version of the manuscript. The original article has been published in final edited form in:

Science Translational Medicine
2021 DEC 01 ; 13(622): eabe8952
doi: 10.1126/scitranslmed.abe8952

Publisher: American Association for the Advancement of Science (AAAS)

Therapeutic inhibition of RBM20 improves diastolic function in a murine heart failure model and human engineered heart tissue

Authors: Michael H. Radke[1,2†], Victor Badillo-Lisakowski[1,2,3†], Thiago Britto-Borges[4,5], Dieter Kubli[6], René Jüttner[1], Pragati Parakkat[1,2,9], Jacobo Lopez Carballo[1,9], Judith Hüttemeister[1,2], Martin Liss[1,2], Arne Hansen[7,8], Christoph Dieterich[4,5], Adam Mullick[6], Michael Gotthardt[1,2,9*]

Affiliations:

[1] Max Delbrück Center for Molecular Medicine in the Helmholtz Association, 13125 Berlin, Germany.

[2] German Center for Cardiovascular Research (DZHK), partner site Berlin, 10785 Berlin, Germany.

[3] Humboldt-Universität zu Berlin, 10099 Berlin, Germany

[4] Section of Bioinformatics and Systems Cardiology, Klaus Tschira Institute for Integrative Computational Cardiology and Department of Internal Medicine III, University Hospital 69120 Heidelberg. Germany

[5] German Center for Cardiovascular Research (DZHK) - Partner site Heidelberg/Mannheim, 69120 Heidelberg, Germany

[6] Ionis Pharmaceuticals, Carlsbad CA 92010, USA.

[7] Department of Experimental Pharmacology and Toxicology, University Medical Center Hamburg-Eppendorf, 20246 Hamburg, Germany.

[8] German Center for Cardiovascular Research (DZHK), Partner Site Hamburg/Kiel/Lübeck, 20246 Hamburg, Germany.

[9] Department of Cardiology, Charité Universitätsmedizin Berlin, 10115 Berlin, Germany

[*] Corresponding author. Email: gotthardt@mdc-berlin.de

[†] These authors contributed equally to this work.

One Sentence Summary: Antisense oligonucleotides targeting RBM20 improve cardiac function in mice with diastolic dysfunction and relaxation in engineered heart tissue.

Abstract: Heart failure with preserved ejection fraction (HFpEF) is prevalent and deadly, but so far, there is no targeted therapy. A main contributor to the disease is impaired ventricular filling, which we improved with antisense oligonucleotides (ASOs) targeting the cardiac splice factor RBM20. In adult mice with increased wall stiffness, weekly application of ASOs over two months increased expression of compliant titin isoforms and improved cardiac function as determined by echocardiography and conductance catheter. RNAseq confirmed RBM20-dependent isoform changes and served as a sensitive indicator of potential side effects, largely limited to genes related to the immune response. We validated our approach in human engineered heart tissue, showing downregulation of RBM20 to less than 50% within 3 weeks of treatment with ASOs, resulting in adapted relaxation kinetics in the absence of cardiac pathology. Our data suggest anti-RBM20 ASOs as powerful cardiac splicing regulators for the causal treatment of human HFpEF.

Introduction

Heart failure is a leading cause of mortality in developed countries. Although several therapeutic options exist, they have proven effective only in heart failure with reduced contractile function as determined by ejection fraction (HFrEF). In heart failure with preserved ejection fraction (HFpEF), where a stiffened ventricle impairs filling, there is no causal therapy *(1)*. More than half of all patients with heart failure belong to this group – predominantly females and the elderly *(2)*.

Factors that affect cardiac filling include collagen of the extracellular matrix and the giant protein titin, which provides the elastic backbone of the myofilament, but neither have been successfully targeted therapeutically in HFpEF *(3)*. Recently, we have identified RBM20 as a splice regulator that determines the elastic, contractile, and electrical properties of the cardiac ventricle *(4)*. Reduced RBM20 activity in mice, rats, and humans leads to altered cardiac filling – in part due to the expression of large titin isoforms with increased compliance *(4–6)*. Accordingly, animal models that replicate phenotypic features of HFpEF, such as increased stiffness of the cardiac ventricle, respond to a 50% reduction in RBM20 expression with improved diastolic filling and improved cardiac function *(7–9)*. In a complementary pharmacological approach, we used a titin splice reporter assay in a small molecule screen and identified cardenolides as efficient RBM20 inhibitors in cell culture *(10)*. As these molecules caused toxicity in vivo at doses required for 50% downregulation of RBM20 activity *(10)*, in the present study we extended our approach to identify antisense oligonucleotides (ASOs) optimized for delivery in vivo and targeting to the heart.

Several animal models of HFpEF have been established using genetics *(11, 12)*, aging *(13)*, and a combination of interventions that affect metabolism and blood pressure *(9, 14)*. Because these models only partially recapitulate human disease, cardiomyocytes derived from induced pluripotent stem cells (iPSC-CM) have been proposed as a tool to custom model HFpEF phenotypes *(15)*. Human iPSC-CM facilitate the evaluation of genetic treatments and antisense approaches for target genes with sequence differences between species, but difficulties to achieve full maturation and to evaluate their mechanical properties under load have so far precluded their utility as a model for HFpEF.

Here, we have identified ASOs that interfere with RBM20 expression and demonstrated their utility in vivo. With weekly injections of palmitoylated ASOs into mice, we were able to adapt diastolic function as determined by echocardiography and conductance catheter. We used iPSC-CM to generate human engineered heart tissue (hEHT), which facilitated the analysis of mechanical properties under load and validated our approach in the human system, and found that altered splicing mediated the therapeutic effect.

Results

Identification and evaluation of RBM20 ASOs that adapt cardiac splicing

Combining in silico and cell-based screening, we identified ASOs that efficiently downregulated the splicing factor RBM20 (Fig. 1A, fig. S1A). In brief, the initial pool of ASO candidates (selected based on in silico safety and activity prediction) was tested in C2C12 cells and filtered to those with potent IC50, a dose-response effect, and predicted low liver toxicity using a machine learning algorithm. We evaluated 20 ASOs after injection into wildtype mice (WT) for their effect on titin splicing in vivo and hepatotoxicity as a common side effect (fig. S1B-E). The most efficient ASO targeted the 3'untranslated region of *Rbm20* and reduced RBM20 expression to less than 50%.

For in vivo toxicity and therapeutic interventions, we used palmitoylated ASOs, based on their improved half-life, activity, and distribution to non-hepatic tissues *(16, 17)*. RBM20 ASO treatment did not affect body- or organ weights, except the spleen (fig. S1F-H), and serum parameters were largely unchanged aside from glucose and triglyceride concentration (Fig. S1I).

To validate the safety of RBM20 ASO treatment, we injected WT mice weekly for a total of 8 weeks to provide sufficient time for side effects to develop. Splicing of the known RBM20 target *Camk2d* was shifted towards the long A isoform (fig. S2A), but there were no signs of arrhythmia (fig. S2B; table S1), no altered contraction and relaxation, and no changes in Ca^{2+} handling in isolated adult cardiomyocytes (fig. S2 C and table S2). The increased sarcomere length in RBM20 ASO treated animals (Table S2) is consistent with the expression of longer titin isoforms (fig. S2 D, E and table S3). There were no signs of fibrosis, hypertrophy or atrophy in trichrome stained heart and skeletal muscle sections from RBM20 ASO-treated animals (fig. S2 F and G).

We evaluated RBM20 as therapeutic target for diastolic dysfunction in the titin N2B knockout mouse with increased titin-based stiffness, reduced trophic signaling, and cardiac atrophy *(18)*. After baseline characterization of cardiac function in WT and titin N2B KO mice, we used weekly injections to evaluate the impact of RBM20 ASOs treatment on cardiac filling and to monitor potential long-term side effects (Fig. 1B). Deep phenotyping after 8 weeks included echocardiography and catheter measurement, RNAseq, and targeted expression profiling.

On the molecular level, RBM20 mRNA and protein expression were downregulated by more than 50% (Fig. 1C-E and fig. S2 H,I), associated with the expected increase in long titin isoforms in the heart (Fig. 1F,G, table S4) that did not result in obvious adverse effects such as altered skeletal muscle mass (fig. S2 J,K,L and table S5). This is unlike previously evaluated small molecule inhibitors of cardiac splicing, which had a lower therapeutic window in cell culture and were unsuitable for downregulation of RBM20 in vivo *(10)*.

RBM20 ASOs restore normal cardiac dimension and improve filling in a mouse model of diastolic dysfunction

Three independent animal models that replicate aspects of HFpEF have validated RBM20 as a therapeutic target - with improved diastolic function after elimination of one *RBM20* allele in all of them *(7–9)*. We opted to use the titin N2B knockout (KO) to assess RBM20 ASO treatment based on the possibility to evaluate diastolic dysfunction as well as cardiac atrophy and the high reproducibility of the phenotype in a genetic vs. an interventional animal model.

After 8 weeks of RBM20 ASO injections we found both improved cardiac function and normalized ventricular dimensions as determined by echocardiography (table S6). This includes left ventricular diameter in diastole, stroke volume and heart weight (Fig. 2A-D, fig. S3). The E to A ratio as a parameter of diastolic function was elevated in the KO but normalized after ASO treatment (Fig. 2E-F). With unchanged body weight, tibia length, heart rate (Fig. 2G), and no indication of arrhythmia (continuous monitoring during echocardiography analysis), we found a <50% increase in spleen weight as the only potential adverse effect. To validate the echocardiography data, we recorded pressure-volume (PV) loops with a conductance catheter (Fig. 3, table S7). Here the ASO effect was stronger in KO vs. WT and comprised restored end-systolic and end diastolic pressures (Fig. 3B-C). Overall, effects on systolic function were less pronounced than effects on diastolic function, with decreased end systolic pressures, decreased dP/dt_{max}, as well as an unchanged end systolic pressure volume relation (Fig. 3D-G). Together, the echocardiography, Doppler, and conductance catheter data reflect improved cardiac function with adapted ventricular filling and normalized cardiac dimensions in N2B KO mice after ASO treatment.

RBM20 ASOs promote expression of embryonic isoforms of substrates involved in sarcomere mechanics and calcium homeostasis

To evaluate the effect size of ASO-mediated RBM20 reduction and potential compensatory secondary changes, we used RNAseq and compared the transcriptomes of WT and N2B KO mice with and without ASO treatment. Of 73 genes differentially spliced after ASO treatment, known substrates of RBM20 include *Ttn* and *Ldb3*, which relate to sarcomere structure, and *Ryr2*, involved in calcium handling *(4, 5)*. Between genotypes, we found 47 differentially spliced genes in WT hearts vs. 51 in N2B KOs, of which 25 were shared (table S8). The top differentially spliced sites are listed in table S9. As expected, we found the strongest effect on exon exclusion (with >80% difference between treatments) in titin's I band region, which determines its elastic properties (Fig. 4A). The effect is consistent with the changes in titin size determined by vertical agarose gel electrophoresis (VAGE) (Fig. 1F, table S5). In addition, RBM20 target exons of *Ldb3*, *Camk2d* and *Ank3* were deregulated after ASO treatment, with similar effects in KO and WT hearts as validated by reverse transcription polymerase chain reaction (RT-PCR) (Fig. 4B-C, Fig. S4). Specifically, there was a switch of *Ldb3* exon 5 vs. 8, while in *Camk2d* E14 was more efficiently included and in *Ank3* E16 and E24, although less efficiently.

ASO treatment induced expression changes relate to differential trophic signaling and an altered immune response

We used RNAseq as a sensitive readout of changes in regulatory networks that indicate adaptations following ASO treatment (fig. S5A). Specifically, we were interested in potential side effects resulting from ASO treatment (present in WT and KO) vs. those resulting from the downregulation of RBM20 (present in ASO-treated and RBM20 knockout mice). We found that changes related to the genotype were less pronounced than those induced by ASO (Fig. 5A). Between WT and KO mice, there was substantial overlap in ASO-responsive genes, which relate to the immune response and metabolism (fig. S5B-C). To focus on potential side effects, we dissected misregulated genes from those reverted to normal expression by ASO treatment (Fig.

5B, table S10). In our disease model, there were 1129 misregulated genes: most of them were associated with immune processes and inflammation (ASO side effects). The remaining deregulated genes predominantly related to cell-substrate adhesion, as previously described in RBM20 N2B double deficient mice (genetic rescue), and were thus ASO independent - attributable to the downregulation of RBM20 *(8)*.

The reversal of the atrophy phenotype (Fig. 5C-F and fig. S5D-G) was based on changes in trophic signaling and associated with metabolic changes (table S11). These changes were similar to those seen with genetic rescue and, although the timeline of the rescue was different (genetics from embryonic development vs. ASO injection into adults), we found a similarly strong effect on hypertrophy markers natriuretic peptide A (*Nppa*) and natriuretic peptide B (*Nppb*), which reflect the reduced stress on the heart (Fig. 5C-D). FHL2 has been linked to cardiac hypertrophy and binds titin's N2B domain, where it acts as a hub for metabolic enzymes *(19)*. Both N2B deficiency and RBM20 knockdown reduce FHL2 protein amount, with a stronger effect of N2B deficiency and the lowest expression observed in the ASO-treated KO (Fig. 5E,F). *Camk2d* was not only differentially spliced after ASO treatment, but protein expression was downregulated specifically in the ASO-treated KO (fig. S5H, I).

Development of human RBM20 ASOs and validation in iPSC-CM and EHT

Selection of human ASOs built on the protocol described for mouse (fig. S1A) with electroporation of human RBM20 ASO into SY5Y cells. The top lead was picked to evaluate the effects of RBM20 downregulation in hiPSC-derived cardiomyocytes and in three-dimensional (3D) engineered heart tissue (EHT). For 2D iPSC-CM, *RBM20* mRNA amount were downregulated to 65% (fig. S6A-B) and *CAMK2D* exon 15 expression was increased after 14 days of treatment with 1 µM ASO, while *LDB3* isoform expression was largely unchanged (fig. S6C-F). Ca^{2+} transients were unchanged after 14 days of ASO treatment, except for a small increase in peak fluorescence normalized to baseline (F_{max}/F_0; 3.44%) and in the length of calcium decay (T_{off}; 2.92%) after 14 days of ASO treatment (fig. S6G-M). As cardiac splicing strongly depends on the developmental stage and differentiation of cardiomyocytes, we refined our validation of the ASO approach using hEHT as a spontaneously beating, human-relevant in vitro model that has been shown to increase cardiomyocyte maturation compared to 2D culture (*20*). Four weeks after 3D hEHT casting, we obtained baseline contractile parameters and started a 3-week treatment by adding 0 (vehicle), 1, or 10 µM RBM20 ASO at every medium change (Fig. 6A). RBM20 expression and predominant nuclear localization in non-treated hEHTs was confirmed by immunofluorescence (Fig. 6B). After 21 days of ASO treatment, both RBM20 mRNA and protein expression were reduced to 52% and 42%, respectively, for 1 µM ASO while 10 µM treatment reduced them to 20% and 21%, respectively (Fig. 6C-E). The gross hEHT morphology and thickness remained unchanged during that time (fig. S7A), and no evidence for arrhythmias was detected when comparing individual beating traces (Fig. 6F) and average RR' scatter values (Fig. 6G). There were no differences in beating frequency, contraction and relaxation forces, or velocities (Fig. 6H and fig. S7B-E). The hEHTs were not electrically paced, therefore the beating frequencies were highly variable within matched measurements and we did not find any ASO-dependent adverse effects. Kinetics of contraction (T1) and relaxation (T2) times were improved. After 3 weeks of treatment, the higher ASO dose induced an 8.9% decrease of early ($T1_{20\%}$) and a 10.2% decrease of mid contraction times ($T1_{50\%}$). Parameters of relaxation were reduced ($T2_{20\%}$ by 7.8%; $T2_{50\%}$ by 10.0% at day 14 and 7.6% vs. 9.4% at day 21,

Fig. 6I-J and fig. S7F-G). We validated the effects of downregulating RBM20 on cardiac isoform expression using *LDB3* and *CAMK2D* as known targets (fig. S7 H-K). Together, the hEHT data suggest that RBM20 ASOs can be used to adapt contraction and relaxation parameters in human cardiomyocytes.

Discussion

Alternative splicing is a main contributor to the diversity of the proteome and human disease *(20)*. For cancer, the clinical relevance of alternative splicing was established more than two decades ago, followed by the evaluation of the spliceosome as a therapeutic target and the development of splice inhibitors that can improve therapeutic response *(21–23)*. The important role of the spliceosome in cardiac disease has been underappreciated, since the majority of splice defects derives from cis effects with mutations in splice sites rather than in splice factors *(24)*. This changed with the identification of RBM20 as a titin splice factor and a potential therapeutic target in HFpEF, as documented in several genetic and interventional animal models *(7–9)*. Here, we chose a genetic model to evaluate ASO treatment of diastolic dysfunction because of its reproducibility. In addition, the N2B knockout mouse provides two independent phenotypic readouts (cardiac atrophy and increased wall stiffness), which both respond to the 50% reduction in RBM20 expression in heterozygous animals *(8)*. Based on this genetic rescue of the N2B KO and lack of secondary mechanical adaptations *(8, 25, 26)*, we expected reduced titin-based stiffness in the adult mouse to translate to improved cardiac filling after ASO treatment, which was indeed what we observed. For cardiac dimensions and weight, we anticipated a difference between preventing atrophy - with reduced RBM20 expression from the onset of cardiac development in the genetic model *(8)* - versus the response of preexisting atrophy to ASO treatment in the adult N2B KO. Surprisingly, ventricular dimensions and heart weight were also partially restored after ASO treatment, providing additional benefit towards improving cardiac function. The molecular basis of the rescue phenotype has been dissected using the genetic approach, where side effects of a therapeutic agent such as the ASO or a small molecule do not obscure the molecular response *(21–23)*.

A main concern with cardiac therapies is the induction of arrhythmia. For RBM20 as a target this is a specific issue, as patients as well as animal models with RBM20 mutations can show signs of atrial fibrillation or ventricular arrhythmia *(27–29)*. This is not the case for the full knockout, where both heterozygotes and homozygotes have a normal electrocardiogram (ECG) *(30)*. The same applies to our genetic rescue with 50% reduction of RBM20 and no signs of arrhythmia *(8)*. Mechanistically, mutations in *Rbm20* not only lead to a reduction in RBM20 activity, but can also cause the formation of RNA granules which have a much more severe effect on cardiac splicing than the downregulation or loss of RBM20 in a conventional knockout *(29)*. The effects on the electrical properties of the heart that result from a mutation in *Rbm20* are thus very different from the effects we see after downregulation of RBM20, and this is reflected in the expected lack of an arrhythmia phenotype with downregulation of RBM20 by ASO.

ASOs have come a long way towards clinical application, exemplified by the global approval of inotersen for treatment of polyneuropathy *(31)* and the analysis of safety and efficacy in patients with transthyretin amyloid cardiomyopathy *(32)*. Their utility in downregulating the splice factor SRSF3 has recently been evaluated in human oral squamous cell carcinoma cells, with improved sensitivity to chemotherapy *(33)*. Here we achieved therapeutic ASO amount in vivo and used RNAseq to confirm the RBM20-dependent isoform changes and as a sensitive indicator of potential side effects. By comparison to the genetic rescue of the N2B KO, we were able to dissect effects resulting from downregulation of RBM20 (shared in both studies) from secondary changes resulting from embryonic RBM20 depletion (in genetic rescue only) and from side effects of the ASO treatment. This information could aid the future development of ASOs with reduced side effects and help identify biomarkers to monitor therapy. The combination of

increased spleen size and deregulation of genes related to the immune response would suggest that interleukin 1b could be a suitable marker to monitor treatment and facilitate ASO development. This would include modified ASOs with palmitate exchanged for peptides or small molecules with affinity to the cardiomyocytes *(16, 17, 32)*, which could further improve the therapeutic window. Nevertheless, even the first generation of RBM20 ASOs were well tolerated specifically compared to small molecule splice inhibitors *(10)*.

Limitations of this study relate to the lack of animal and cell based models that capture the broad spectrum of human HFpEF phenotypes. Towards evaluating therapeutic relevance, we used iPSC-derived cardiomyocytes and engineered heart tissue to confirm the effect of ASOs directed against human *RBM20*. EHTs have previously been used to evaluate toxicity of small molecules, disease relevance of human mutations and for drug screening *(34–36)*. EHT-based models of HFpEF do not exist, but we successfully utilized naïve EHTs to evaluate the effect of RBM20 ASOs on contraction and relaxation kinetics. RBM20 ASOs efficiently penetrated human cardiomyocytes in the 3D-culture and downregulated RBM20 by 50% at 1 µM with no obvious adverse effect. Although EHTs generated with current technology do not reach the maturity of adult cardiomyocytes in vivo, the expression of N2B and N2BA isoforms is sufficient to validate the effects of RBM20 *(37)*. Indeed, we were able to improve contraction and relaxation kinetics and confirmed the effect of RBM20 ASO on two additional known substrates, one of which (CAMK2D) also contributes to diastolic function *(38, 39)*. In the future, we will benefit from more mature iPSC-derived cardiomyocytes *(40, 41)*, the development of EHTs that better capture the contribution of non-cardiomyocytes and a stiff extracellular matrix *(36)*, as well as complex interventional HFpEF animal models *(14)*.

Materials and Methods

Study design

This study was designed to assess the therapeutic potential of RBM20 antisense oligonucleotides (ASO) to treat diastolic dysfunction. Mouse and human RBM20 ASO were designed in silico and validated in cell culture experiments. Potential side effects of RBM20-ASO treatment were evaluated in wildtype mice and therapeutic potential in a mouse model with diastolic dysfunction (titin N2B KO). Animals underwent echocardiography before and 8 weeks after the ASO treatment started. After the final echocardiography, ECG and conductance catheter measurement, tissues were harvested for molecular and morphological analysis and cells for single cardiomyocyte contraction and Ca^{2+} measurements. Human relevance was evaluated in human engineered heart tissue (hEHT) after 3 weeks of treatment. Molecular analyses (RNA isoform and protein expression) included RNA-sequencing, real time PCR and Western blot or WES.

All experiments involving animals were carried out following the Guide for the Care and Use of Laboratory Animals of the German animal welfare act and guidelines from American Association for the Accreditation of Laboratory animal care, and the ARRIVE guidelines. Protocols were approved by the Committee on the Ethics of Animal Experiments of Berlin State authorities (LAGeSo) or by the Animal Welfare Committee (Cold Spring Harbor Laboratory's Institutional Animal Care and Use Committee guidelines). Animals were housed in individually ventilated cages with free access to food and water and a 12h:12h light/dark cycle at 22±2°C and 55±10% humidity. For power calculations to estimate we used G*Power 3.1 *(42)*. For ECG, echocardiography and catheter measurements, researchers were blinded to the treatment groups. Individual subject-level values where data are shown as group averages are listed in data file S1.

RBM20 ASO screen and selection

A pool of ASO candidates with >70% probability of being active and safe (low liver toxicity) were designed. Top candidates were selected for an in vitro single-dose (3 μM for mouse, 2 μM for human) electroporation screen in C2C12 (mouse) or SH-SY5Y (human) cells (ATCC). The most active compounds were evaluated in vitro in a dose-response screen. Mouse ASOs with IC50 ≤ 0.6 μM were selected for in vivo evaluation of activity and tolerability. The 3 top candidates (most active with lowest liver transaminase signal) were modified by palmitate conjugation to improve activity and reevaluated in a second in vivo study. ASO 32C (palmitate-conjugated) was selected based on the safety and activity profile.

RBM20 ASO treatment

Male wildtype (WT) and titin N2B knockout (KO) mice were maintained on a 129S6 background (Taconic). Mice for toxicity studies were on a C57BL/6 background (Jackson Laboratories). At 8 weeks of age mice were subcutaneously injected with 50 mg/kg/week RBM20 ASO (1052591; RBM20_32; TACTATGATGCATGGA) for 8 weeks (Fig. 1A) or vehicle control. Following 3R principles (Replacement, Reduction and Refinement),we only used one control group and prioritized vehicle over scrambled ASO, as the latter would have masked generic ASO side effects such as changes in glucose and triglyceride concentrations.

ECG

Wildtype mice were anesthetized with oxygen and 2% isoflurane, the ECG recordings were done with needle electrodes. For ECG analysis we used Power Lab 8/30 with Octal Bio Amp (ADInstruments) with LabChart V8.1.16.12.2019 and evaluated an average of 100-120 beats on derivation II.

Echocardiography
For echocardiography, age- and sex-matched mice were anesthetized with an intermixture of oxygen and 2.5% isoflurane. The fur was removed using a hair removal cream and a shaver. Contact gel was used for optimal imaging of the transducer. Vital parameters such as heart rate and breathing frequency were measured using electrodes at the paws. The ultrasonic probe MS-400 was used to determine the cardiac parameters and the VEVO 2100 system (Visualsonics Fujifilm) for visualization as described previously *(25)*.

Conductance catheter measurement
For cardiac pressure and volume measurements the Millar Conductance Catheter System was used as described previously *(25)*. For anesthesia with oxygen and 2.5% isoflurane, animals were orotracheally intubated and ventilated. The catheter was inserted retrogradely into the left ventricle via the *arteria carotis communis* to measure pressure volume relations. The artery was exposed by cervical incision between the lower jaw and sternum. Blood was arrested proximal and distal of the artery. The placement of the catheter was validated by electrocardiography (Vevo 2100). Pressure independent parameters were measured after a three second occlusion of the vena cava inferior. The vein was exposed by opening the peritoneum. The occlusion causes a pressure decrease and a reduction of the left ventricular volume. The procedure was repeated 3 to 5 times with 2 min between maneuvers. Five representative loops were selected to calculate end diastolic pressure volume relation (EDPVR) and end systolic pressure volume relation (ESPVR) *(43)*.

Isolation and calcium imaging of adult mouse cardiomyocytes
Adult mouse cardiomyocytes were prepared after 8 weeks of RBM20 ASO or phosphate buffered saline (PBS) treatment. Hearts were excised and digested via retrograde perfusion with liberase (Roche) *(44)*. Cells were loaded with 0.2 µM Fura-2/AM (F1221, Life technologies), incubated for 30 minutes at 37°C and subsequently washed in recording buffer containing (in mM) 135 NaCl, 4 KCl, 10 Hepes, 5 glucose, 1.8 $CaCl_2$, 1 $MgCl_2$, pH 7.3, 300 mOsmol/kg. Contractile and Ca^{2+} parameters were collected with the CytoCypher MultiCell High Throughput System (IonOptix). Cells were measured at 25° C and were electrically stimulated with 10 V at 1 Hz (bipolar pulse 5 ms) with a MyoPacer MYP100 (IonOptix). FFT-based sarcomere length data and Ca^{2+} transients were recorded at 250 Hz using IonWizard data acquisition software (IonOptix) and calculated by CytoSolver Desktop (IonOptix). The robust regression and outlier removal (ROUT) method (Q = 1%) was used to identify outliers. Data were analyzed with the Mann-Whitney test and presented as mean ± SD.

Histology of heart and skeletal muscle
After 8 weeks of ASO or PBS treatment mice were killed and perfused with 4% paraformaldehyde (PFA) in PBS. After overnight fixation the tissue was embedded in paraffin and 8 µm sections were stained with Masson's Trichrome stain (Sigma). Pictures were taken on a Leica DMI6000 microscope.

Blood and tissue biochemistry
Animals were killed by cervical dislocation. Hearts were removed, frozen in liquid nitrogen and stored at -80°C. Blood was collected by cardiac puncture exsanguination with K_2-EDTA (Becton Dickinson Franklin Lakes, NJ, USA) and plasma separated by centrifugation at 10 000 rcf for 4 min at 4°C. Plasma transaminases were measured using a Beckman Coulter AU480 analyzer. Tissues were collected, weighed, flash frozen on liquid nitrogen and stored at −80°C.

Human induced pluripotent stem cells
Expansion and cardiac differentiation of human induced pluripotent stem cells (hiPSCs, C25 line *(45)* kind gift from Alessandra Moretti, Munich, Germany) was performed as described *(46)*. In brief, hiPSCs were expanded in FTDA media *(47)* on Geltrex-coated cell culture vessels. Splitting was performed in 3.5 day intervals with EDTA. Embryoid bodies were generated in spinner flasks, and differentiation was induced by the administration of growth factors and small molecules to induce mesodermal progenitors (3 ng/ml activin-A, 10 ng/ml BMP-4 and 5 ng/ml basic FGF), cardiac progenitors, and cardiomyocytes. For differentiation, we used Pluronic F-127-coated cell culture vessels. Differentiated cardiomyocytes were dissociated with collagenase, analyzed by flow cytometry for cardiac differentiation efficiency (cardiac troponin T, minimum 70% positivity), and used to generate 3D engineered heart tissue (EHT).

Cardiac differentiation of iPSCs for Ca^{2+} imaging
Single-cell dissociated hiPSCs (BIHi005-A line) were seeded on Geltrex-coated plates and maintained in E8 media (Gibco). Three days post splitting, cells with 80-90% confluency were selected for cardiac differentiation and maintained in RPMI 1640 GlutaMAX Hepes (Gibco) + B27 minus insulin (Gibco) media. At day 0, cells were subjected to mesoderm induction with 4µM CHIR99021 (Sigma) followed by cardiac priming at day 3 with 5µM IWP2 (Merck Millipore). Robustly contracting iPSC-CM were metabolically selected at day 11 with lactate selection media for 2-3 days. Purified iPSC-CM were digested at day 25 and day 60, and were maintained in RPMI GlutaMax Hepes + B27 media.

Ca^{2+} imaging of iPSC-derived cardiomyocytes
Day 95 iPSC-CM were digested on Geltrex-coated coverslips and let to recover for 4 days before starting calcium transient recordings. Changes in intracellular Ca^{2+} concentrations in day 100 iPSC-CM were recorded during paced contractions. The cells were recorded at baseline and after 2 weeks of vehicle control (PBS) or 1 µM RBM20 ASO treatment. Cardiomyocytes in culture medium were loaded with 0.2 µM Ca^{2+}-sensitive indicator Fura-2/AM and washed with recording buffer and let to recover for 30 min, as done for the mouse cardiomyocytes (see above). Fluorescence measurements were performed with a Polychrome V (Till Photonics) monochromator and a camera (ANDOR Clara DR-01854, ANDOR technology) operated by Live Acquisition software (Till Photonics). Cells were exposed to alternating excitation light pulses of 340 nm and 380 nm wavelengths for 40 ms or 15 ms at intervals of 80 ms (12.5 Hz) for 30 sec and paced by MyoPacer MYP100 (IonOptix) at 0.5 Hz (20 V, bipolar pulse, 2 ms). Emission images were collected at 510 nm. Images were obtained using a 40x (Zeiss) objective. Fluorescence intensities were taken from user-defined regions of interest (ROI´s) representing single cardiomyocytes and presented as F/F_0, where F represents the ratio 340/380 nm, which is related to the intracellular Ca^{2+} concentration. Data from Ca^{2+}-transients were calculated using CalTrack, a MATLAB (MathWorks) based algorithm *(48)*.

Human engineered heart tissue (hEHT)
Generation, maintenance, and video-optical contractility analysis of hEHTs has been described *(46, 49)*. In brief, $1x10^6$ human iPSC-derived cardiomyocytes per assembly were cast within a fibrin-based hEHT in a 24-well strip format and cultured under auxotonic load at 37°C, 40% O_2 and 7% CO_2 with alternating daily hEHT medium change. After 4 weeks of hEHT culture, treatment with 0 (vehicle control), 1, or 10 µM ASO was randomly assigned to 4 hEHTs per group and added in 15 µl fresh medium. After 1h equilibration, continuous video-optical recordings were started following default parameters for hEHTs and repeated at days 7, 14 and

21 after ASO treatment. ASOs were freshly added with every medium change during the experiment. After the last recording at day 21, the hEHTs were harvested for molecular analyses.

RNA and protein expression analysis

Frozen hEHTs were separated into two tissue pieces for RNA and protein extraction. The heart tissue was ground to a powder with mortar and pestle under liquid nitrogen and used for subsequent RNA and protein expression analysis. RNAseq library prep was performed as described *(8)*. RNA was extracted with TRIzol (Thermo Fisher) using the manufacturer's protocol with an additional step of homogenization using TissueLyser II (Qiagen) at 25 Hz for 45 seconds. The RNA was treated with DNase I (Fermentas) for 30 minutes at room temperature and purified with RNeasy MinElute Cleanup Kit (Qiagen). For cDNA synthesis, we used High-Capacity cDNA Reverse Transcription Kit (Applied Biosystems). Splicing PCR to detect differentially included exons followed Taq DNA polymerase PCR kit (New England Biolabs) instructions. PCR bands were sequenced with h*LDB3*_E3_fwd and h*CAMK2D*_E12_fwd primers for exon calling. Primers are provided in table S12. RT-PCR gel densitometry was calculated with ImageJ v1.53a. For protein extraction, hEHTs were incubated on ice for 20 minutes in RIPA buffer supplemented with cOmplete, Mini, EDTA-free Protease Inhibitor Cocktail (Roche) and PhosSTOP (Sigma). Each piece was homogenized with TissueLyser II followed by sonication with VialTweeter (Hielscher) at 70% amplitude, 0.5 pulse cycle during 20 pulses and centrifuged at 13.000 rpm and 4°C. Protein supernatant concentration was measured with the BCA Protein Assay Kit (Pierce). Titin isoforms were analyzed using vertical agarose gel electrophoresis as described previously *(50)*.

RNAseq data analysis

Differential gene expression was analyzed as described previously *(8)*. Differential splicing analysis was computed with Leafcutter *(51)*, R version 3.6.1, and Leafcutter version 0.2.9), with the parameters *--min_samples_per_group* and *--min_samples_per_intron* set to 2. Intron clusters with an adjusted p-value < 0.05 and |deltapsi| > 0.1 were called significant, and only the splice junctions in the selected cluster were further analyzed. Sashimi plots were generated with a modified version of ggsashimi *(52)*, version 0.4.0) with the *--min-coverage* parameter set to 10. To obtain the splice junction read counts for novel and annotated exons, we proceed with *de novo* transcriptome assembly with StringTie version 1.3.5 *(53)* using the following parameters *minimum isoform fraction* set to 0.2, *minimum anchor length for junctions* to 8, *minimum junction coverage* to 3 and in the guided mode. The splice junction counts and exon structure were obtained from STAR *SJ.out.tab* file and StringTie, respectively. Next, we plotted the PSI values for transcripts in a modified version of the *Mus musculus* reference genome GRCm38.84, and canonical transcripts were used as representative for their respective genes. This workflow is available and detailed at *(54)*.

Quantitative real-time PCR

The RT-qPCR was performed as described in a multiplex reaction *(55)*. For normalization, we used mouse *Eef1a1* or 18S and human *ACTN2* as indicated. Information on primers and amplicons is listed in tables S13 and S14.

WES protein detection

We used the WES system (ProteinSimple) for protein detection and quantification following the manufacturer's instructions. Protein samples were resolved in RIPA buffer and used at 0.2mg/ml for tissue and 0.25 mg/ml for EHT. After separation by capillary electrophoresis, proteins are

crosslinked to the capillary wall and detected by incubating and washing with primary and secondary antibodies. Antibodies are listed in table S15.

Western blot

Proteins were separated on an SDS-PAGE. Western blot was performed on PVDF membranes. The anti-FHL1 and tubulin antibodies are listed in table S15. The secondary HRP-conjugated antibody was detected by chemiluminescence staining with ECL (Supersignal West Femto Chemiluminescent Substrate; Pierce Chemical Co.) on a FusionFX system, and quantification of blots were performed with AIDA software v 4.19.

Immunofluorescence

Frozen hEHT tissue blocks were sectioned at 4 µm thickness with CryoStar NX70 cryostat , fixed in 4% PFA, washed twice in PBS and blocked with goat serum, 0.3% Triton X and 0.2% bovine serum albumin (BSA). The sections were incubated over night at 4°C with anti-RBM20 and a-actinin primary antibodies, washed five times in PBS and incubated for 2h at room temperature in the dark with 1:1000 4′,6-diamidino-2-phenylindole (DAPI) staining and secondary antibodies. The slides were mounted with Dako Fluorescence Mounting Medium (Agilent) and imaged as described below for iPSC-CM. 95-day-old iPSC CMs seeded on Geltrex-coated coverslips were fixed with 4% PFA, staining protocol follows as above. The coverslips were mounted with Fluromount-G (Invitrogen) and imaged with 60X oil immersion objective from Delta Vision Elite Deconvolution Microscope (GE Life Sciences). Images were processed with ImageJ v1.52/Fiji. Antibodies are listed in table S16.

Statistical Analysis

Graph Pad Prism software (v6.01) was used for statistical analysis. Data are displayed as means ± SEM. Two groups were compared with unpaired, two-tailed t tests, multiple groups with one-way or two-way ANOVA depending on the number of grouping variables (treatment only or treatment versus genotype), followed by Tukey's multiple comparison post-test. P-value and the number of biological replicates (n) is indicated in each figure legend. A p-value (P) <0.05 was considered as statistically significant.

Supplementary Materials

Figs. S1 to S7

Tables S1 to S16

Data file S1

References and Notes:

1. S. J. Shah, B. A. Borlaug, D. W. Kitzman, A. D. McCulloch, B. C. Blaxall, R. Agarwal, J. A. Chirinos, S. Collins, R. C. Deo, M. T. Gladwin, H. Granzier, S. L. Hummel, D. A. Kass, M. M. Redfield, F. Sam, T. J. Wang, P. Desvigne-Nickens, B. B. Adhikari, Research Priorities for Heart Failure With Preserved Ejection Fraction: National Heart, Lung, and Blood Institute Working Group Summary, *Circulation* **141**, 1001–1026 (2020).

2. O. Chioncel, M. Lainscak, P. M. Seferovic, S. D. Anker, M. G. Crespo-Leiro, V.-P. Harjola, J. Parissis, C. Laroche, M. F. Piepoli, C. Fonseca, A. Mebazaa, L. Lund, G. A. Ambrosio, A. J. Coats, R. Ferrari, F. Ruschitzka, A. P. Maggioni, G. Filippatos, Epidemiology and one-year outcomes in patients with chronic heart failure and preserved, mid-range and reduced ejection fraction: an analysis of the ESC Heart Failure Long-Term Registry, *Eur. J. Heart Fail.* **19**, 1574–1585 (2017).

3. P. M. Seferović, M. Polovina, J. Bauersachs, M. Arad, T. B. Gal, L. H. Lund, S. B. Felix, E. Arbustini, A. L. P. Caforio, D. Farmakis, G. S. Filippatos, E. Gialafos, V. Kanjuh, G. Krljanac, G. Limongelli, A. Linhart, A. R. Lyon, R. Maksimović, D. Miličić, I. Milinković, M. Noutsias, A. Oto, Ö. Oto, S. U. Pavlović, M. F. Piepoli, A. D. Ristić, G. M. C. Rosano, H. Seggewiss, M. Ašanin, J. P. Seferović, F. Ruschitzka, J. Čelutkiene, T. Jaarsma, C. Mueller, B. Moura, L. Hill, M. Volterrani, Y. Lopatin, M. Metra, J. Backs, W. Mullens, O. Chioncel, R. A. de Boer, S. Anker, C. Rapezzi, A. J. S. Coats, C. Tschöpe, Heart failure in cardiomyopathies: a position paper from the Heart Failure Association of the European Society of Cardiology, *Eur. J. Heart Fail.* **21**, 553–576 (2019).

4. W. Guo, S. Schafer, M. L. Greaser, M. H. Radke, M. Liss, T. Govindarajan, H. Maatz, H. Schulz, S. Li, A. M. Parrish, V. Dauksaite, P. Vakeel, S. Klaassen, B. Gerull, L. Thierfelder, V. Regitz-Zagrosek, T. A. Hacker, K. W. Saupe, G. W. Dec, P. T. Ellinor, C. A. MacRae, B. Spallek, R. Fischer, A. Perrot, C. Özcelik, K. Saar, N. Hubner, M. Gotthardt, RBM20, a gene for hereditary cardiomyopathy, regulates titin splicing, *Nat. Med.* **18**, 766–773 (2012).

5. H. Maatz, M. Jens, M. Liss, S. Schafer, M. Heinig, M. Kirchner, E. Adami, C. Rintisch, V. Dauksaite, M. H. Radke, M. Selbach, P. J. R. Barton, S. A. Cook, N. Rajewsky, M. Gotthardt, M. Landthaler, N. Hubner, RNA-binding protein RBM20 represses splicing to orchestrate cardiac pre-mRNA processing, *J. Clin. Invest.* **124**, 3419–3430 (2014).

6. M. Methawasin, K. R. Hutchinson, E.-J. Lee, J. E. Smith, C. Saripalli, C. G. Hidalgo, C. A. C. Ottenheijm, H. Granzier, Experimentally increasing titin compliance in a novel mouse model attenuates the Frank-Starling mechanism but has a beneficial effect on diastole, *Circulation* **129**, 1924–1936 (2014).

7. M. Bull, M. Methawasin, J. Strom, P. Nair, K. Hutchinson, H. Granzier, Alternative Splicing of Titin Restores Diastolic Function in an HFpEF-Like Genetic Murine Model (TtnΔIAjxn), *Circ. Res.* **119**, 764–772 (2016).

8. F. Hinze, C. Dieterich, M. H. Radke, H. Granzier, M. Gotthardt, Reducing RBM20 activity improves diastolic dysfunction and cardiac atrophy, *J. Mol. Med.* **94**, 1349–1358 (2016).

9. M. Methawasin, J. G. Strom, R. E. Slater, V. Fernandez, C. Saripalli, H. Granzier, Experimentally Increasing the Compliance of Titin Through RNA Binding Motif-20 (RBM20) Inhibition Improves Diastolic Function In a Mouse Model of Heart Failure With Preserved Ejection Fraction, *Circulation* **134**, 1085–1099 (2016).

10. M. Liss, M. H. Radke, J. Eckhard, M. Neuenschwander, V. Dauksaite, J.-P. von Kries, M. Gotthardt, Drug discovery with an RBM20 dependent titin splice reporter identifies cardenolides as lead structures to improve cardiac filling, *PloS One* **13**, e0198492 (2018).

11. B. Bai, W. Yang, Y. Fu, H. L. Foon, W. T. Tay, K. Yang, C. Luo, J. Gunaratne, P. Lee, M. R. Zile, A. Xu, C. W. L. Chin, C. S. P. Lam, W. Han, Y. Wang, Seipin Knockout Mice Develop Heart Failure With Preserved Ejection Fraction, *JACC Basic Transl. Sci.* **4**, 924–937 (2019).

12. K. Yousefi, C. I. Irion, L. M. Takeuchi, W. Ding, G. Lambert, T. Eisenberg, S. Sukkar, H. L. Granzier, M. Methawasin, D. I. Lee, V. Hahn, D. A. Kass, K. E. Hatzistergos, J. M. Hare, K. A. Webster, L. A. Shehadeh,

Osteopontin Promotes Left Ventricular Diastolic Dysfunction through a Mitochondrial Pathway, *J. Am. Coll. Cardiol.* **73**, 2705–2718 (2019).

13. J. D. Roh, N. Houstis, A. Yu, B. Chang, A. Yeri, H. Li, R. Hobson, C. Lerchenmüller, A. Vujic, V. Chaudhari, F. Damilano, C. Platt, D. Zlotoff, R. T. Lee, R. Shah, M. Jerosch-Herold, A. Rosenzweig, Exercise training reverses cardiac aging phenotypes associated with heart failure with preserved ejection fraction in male mice, *Aging Cell* **19**, e13159 (2020).

14. G. G. Schiattarella, F. Altamirano, D. Tong, K. M. French, E. Villalobos, S. Y. Kim, X. Luo, N. Jiang, H. I. May, Z. V. Wang, T. M. Hill, P. P. A. Mammen, J. Huang, D. I. Lee, V. S. Hahn, K. Sharma, D. A. Kass, S. Lavandero, T. G. Gillette, J. A. Hill, Nitrosative stress drives heart failure with preserved ejection fraction, *Nature* **568**, 351–356 (2019).

15. E. R. Porrello, L. M. D. Delbridge, HFpEF-Time to Explore the Role of Genetic Heterogeneity in Phenotypic Variability: New Mechanistic Insights Offer Promise for Personalized Therapies, *Circulation* **140**, 1607–1609 (2019).

16. T. P. Prakash, A. E. Mullick, R. G. Lee, J. Yu, S. T. Yeh, A. Low, A. E. Chappell, M. E. Østergaard, S. Murray, H. J. Gaus, E. E. Swayze, P. P. Seth, Fatty acid conjugation enhances potency of antisense oligonucleotides in muscle, *Nucleic Acids Res.* **47**, 6029–6044 (2019).

17. M. E. Østergaard, M. Jackson, A. Low, A. E Chappell, R. G Lee, R. Q. Peralta, J. Yu, G. A. Kinberger, A. Dan, R. Carty, M. Tanowitz, P. Anderson, T.-W. Kim, L. Fradkin, A. E. Mullick, S. Murray, F. Rigo, T. P. Prakash, C. F. Bennett, E. E. Swayze, H. J. Gaus, P. P. Seth, Conjugation of hydrophobic moieties enhances potency of antisense oligonucleotides in the muscle of rodents and non-human primates, *Nucleic Acids Res.* **47**, 6045–6058 (2019).

18. M. H. Radke, J. Peng, Y. Wu, M. McNabb, O. L. Nelson, H. Granzier, M. Gotthardt, Targeted deletion of titin N2B region leads to diastolic dysfunction and cardiac atrophy, *Proc. Natl. Acad. Sci. U. S. A.* **104**, 3444–3449 (2007).

19. S. Lange, D. Auerbach, P. McLoughlin, E. Perriard, B. W. Schäfer, J.-C. Perriard, E. Ehler, Subcellular targeting of metabolic enzymes to titin in heart muscle may be mediated by DRAL/FHL-2, *J. Cell Sci.* **115**, 4925–4936 (2002).

20. M. M. Scotti, M. S. Swanson, RNA mis-splicing in disease, *Nat. Rev. Genet.* **17**, 19–32 (2016).

21. M. Seiler, A. Yoshimi, R. Darman, B. Chan, G. Keaney, M. Thomas, A. A. Agrawal, B. Caleb, A. Csibi, E. Sean, P. Fekkes, C. Karr, V. Klimek, G. Lai, L. Lee, P. Kumar, S. C.-W. Lee, X. Liu, C. Mackenzie, C. Meeske, Y. Mizui, E. Padron, E. Park, E. Pazolli, S. Peng, S. Prajapati, J. Taylor, T. Teng, J. Wang, M. Warmuth, H. Yao, L. Yu, P. Zhu, O. Abdel-Wahab, P. G. Smith, S. Buonamici, H3B-8800, an orally available small-molecule splicing modulator, induces lethality in spliceosome-mutant cancers, *Nat. Med.* **24**, 497–504 (2018).

22. D. Aird, T. Teng, C.-L. Huang, E. Pazolli, D. Banka, K. Cheung-Ong, C. Eifert, C. Furman, Z. J. Wu, M. Seiler, S. Buonamici, P. Fekkes, C. Karr, J. Palacino, E. Park, P. G. Smith, L. Yu, Y. Mizui, M. Warmuth, A. Chicas, L. Corson, P. Zhu, Sensitivity to splicing modulation of BCL2 family genes defines cancer therapeutic strategies for splicing modulators, *Nat. Commun.* **10**, 137 (2019).

23. S. C.-W. Lee, H. Dvinge, E. Kim, H. Cho, J.-B. Micol, Y. R. Chung, B. H. Durham, A. Yoshimi, Y. J. Kim, M. Thomas, C. Lobry, C.-W. Chen, A. Pastore, J. Taylor, X. Wang, A. Krivtsov, S. A. Armstrong, J. Palacino, S. Buonamici, P. G. Smith, R. K. Bradley, O. Abdel-Wahab, Modulation of splicing catalysis for therapeutic targeting of leukemia with mutations in genes encoding spliceosomal proteins, *Nat. Med.* **22**, 672–678 (2016).

24. A. Beqqali, Alternative splicing in cardiomyopathy, *Biophys. Rev.* **10**, 1061–1071 (2018).

25. H. L. Granzier, M. H. Radke, J. Peng, D. Westermann, O. L. Nelson, K. Rost, N. M. P. King, Q. Yu, C. Tschöpe, M. McNabb, D. F. Larson, S. Labeit, M. Gotthardt, Truncation of titin's elastic PEVK region leads to cardiomyopathy with diastolic dysfunction, *Circ. Res.* **105**, 557–564 (2009).

26. J. Nedrud, S. Labeit, M. Gotthardt, H. Granzier, Mechanics on Myocardium Deficient in the N2B Region of Titin: The Cardiac-Unique Spring Element Improves Efficiency of the Cardiac Cycle, *Biophys. J.* **101**, 1385–1392 (2011).

27. K. M. Brauch, M. L. Karst, K. J. Herron, M. de Andrade, P. A. Pellikka, R. J. Rodeheffer, V. V. Michels, T. M. Olson, Mutations in ribonucleic acid binding protein gene cause familial dilated cardiomyopathy, *J. Am. Coll. Cardiol.* **54**, 930–941 (2009).

28. M. M. G. van den Hoogenhof, A. Beqqali, A. S. Amin, I. van der Made, S. Aufiero, M. A. F. Khan, C. A. Schumacher, J. A. Jansweijer, K. Y. van Spaendonck-Zwarts, C. A. Remme, J. Backs, A. O. Verkerk, A. Baartscheer, Y. M. Pinto, E. E. Creemers, RBM20 Mutations Induce an Arrhythmogenic Dilated Cardiomyopathy Related to Disturbed Calcium Handling, *Circulation* **138**, 1330–1342 (2018).

29. J. W. Schneider, S. Oommen, M. Y. Qureshi, S. C. Goetsch, D. R. Pease, R. S. Sundsbak, W. Guo, M. Sun, H. Sun, H. Kuroyanagi, D. A. Webster, A. W. Coutts, K. A. Holst, B. S. Edwards, N. Newville, M. A. Hathcock, T. Melkamu, F. Briganti, W. Wei, M. G. Romanelli, S. C. Fahrenkrug, D. E. Frantz, T. M. Olson, L. M. Steinmetz, D. F. Carlson, T. J. Nelson, Wanek Program Preclinical Pipeline, Dysregulated ribonucleoprotein granules promote cardiomyopathy in RBM20 gene-edited pigs, *Nat. Med.* **26**, 1788–1800 (2020).

30. K. Ihara, T. Sasano, Y. Hiraoka, M. Togo-Ohno, Y. Soejima, M. Sawabe, M. Tsuchiya, H. Ogawa, T. Furukawa, H. Kuroyanagi, A missense mutation in the RSRSP stretch of Rbm20 causes dilated cardiomyopathy and atrial fibrillation in mice, *Sci. Rep.* **10**, 17894 (2020).

31. D. Adams, A. Gonzalez-Duarte, W. D. O'Riordan, C.-C. Yang, M. Ueda, A. V. Kristen, I. Tournev, H. H. Schmidt, T. Coelho, J. L. Berk, K.-P. Lin, G. Vita, S. Attarian, V. Planté-Bordeneuve, M. M. Mezei, J. M. Campistol, J. Buades, T. H. Brannagan, B. J. Kim, J. Oh, Y. Parman, Y. Sekijima, P. N. Hawkins, S. D. Solomon, M. Polydefkis, P. J. Dyck, P. J. Gandhi, S. Goyal, J. Chen, A. L. Strahs, S. V. Nochur, M. T. Sweetser, P. P. Garg, A. K. Vaishnaw, J. A. Gollob, O. B. Suhr, Patisiran, an RNAi Therapeutic, for Hereditary Transthyretin Amyloidosis, *N. Engl. J. Med.* **379**, 11–21 (2018).

32. M. D. Benson, N. R. Dasgupta, S. M. Rissing, J. Smith, H. Feigenbaum, Safety and efficacy of a TTR specific antisense oligonucleotide in patients with transthyretin amyloid cardiomyopathy, *Amyloid* **24**, 219–225 (2017).

33. Y. Sun, L. Yan, J. Guo, J. Shao, R. Jia, Downregulation of SRSF3 by antisense oligonucleotides sensitizes oral squamous cell carcinoma and breast cancer cells to paclitaxel treatment, *Cancer Chemother. Pharmacol.* **84**, 1133–1143 (2019).

34. J. T. Hinson, A. Chopra, N. Nafissi, W. J. Polacheck, C. C. Benson, S. Swist, J. Gorham, L. Yang, S. Schafer, C. C. Sheng, A. Haghighi, J. Homsy, N. Hubner, G. Church, S. A. Cook, W. A. Linke, C. S. Chen, J. G. Seidman, C. E. Seidman, Titin mutations in iPS cells define sarcomere insufficiency as a cause of dilated cardiomyopathy, *Science* **349**, 982–986 (2015).

35. R. J. Mills, B. L. Parker, G. A. Quaife-Ryan, H. K. Voges, E. J. Needham, A. Bornot, M. Ding, H. Andersson, M. Polla, D. A. Elliott, L. Drowley, M. Clausen, A. T. Plowright, I. P. Barrett, Q.-D. Wang, D. E. James, E. R. Porrello, J. E. Hudson, Drug Screening in Human PSC-Cardiac Organoids Identifies Pro-proliferative Compounds Acting via the Mevalonate Pathway, *Cell Stem Cell* **24**, 895-907.e6 (2019).

36. Y. Zhao, N. Rafatian, N. T. Feric, B. J. Cox, R. Aschar-Sobbi, E. Y. Wang, P. Aggarwal, B. Zhang, G. Conant, K. Ronaldson-Bouchard, A. Pahnke, S. Protze, J. H. Lee, L. Davenport Huyer, D. Jekic, A. Wickeler, H. E. Naguib, G. M. Keller, G. Vunjak-Novakovic, U. Broeckel, P. H. Backx, M. Radisic, A Platform for Generation of Chamber-Specific Cardiac Tissues and Disease Modeling, *Cell* **176**, 913-927.e18 (2019).

37. K. Streckfuss-Bömeke, M. Tiburcy, A. Fomin, X. Luo, W. Li, C. Fischer, C. Özcelik, A. Perrot, S. Sossalla, J. Haas, R. O. Vidal, S. Rebs, S. Khadjeh, B. Meder, S. Bonn, W. A. Linke, W.-H. Zimmermann, G. Hasenfuss, K. Guan, Severe DCM phenotype of patient harboring RBM20 mutation S635A can be modeled by patient-specific induced pluripotent stem cell-derived cardiomyocytes, *J. Mol. Cell. Cardiol.* **113**, 9–21 (2017).

38. C. G. Hidalgo, C. S. Chung, C. Saripalli, M. Methawasin, K. R. Hutchinson, G. Tsaprailis, S. Labeit, A. Mattiazzi, H. L. Granzier, The multifunctional Ca(2+)/calmodulin-dependent protein kinase II delta (CaMKIIδ) phosphorylates cardiac titin's spring elements, *J. Mol. Cell. Cardiol.* **54**, 90–97 (2013).

39. N. Hamdani, J. Krysiak, M. M. Kreusser, S. Neef, C. G. Dos Remedios, L. S. Maier, M. Krüger, J. Backs, W. A. Linke, Crucial role for Ca2(+)/calmodulin-dependent protein kinase-II in regulating diastolic stress of normal and failing hearts via titin phosphorylation, *Circ. Res.* **112**, 664–674 (2013).

40. K. Ronaldson-Bouchard, S. P. Ma, K. Yeager, T. Chen, L. Song, D. Sirabella, K. Morikawa, D. Teles, M. Yazawa, G. Vunjak-Novakovic, Advanced maturation of human cardiac tissue grown from pluripotent stem cells, *Nature* **556**, 239–243 (2018).

41. J. M. Bliley, M. C. S. C. Vermeer, R. M. Duffy, I. Batalov, D. Kramer, J. W. Tashman, D. J. Shiwarski, A. Lee, A. S. Teplenin, L. Volkers, B. Coffin, M. F. Hoes, A. Kalmykov, R. N. Palchesko, Y. Sun, J. D. H. Jongbloed, N. Bomer, R. A. de Boer, A. J. H. Suurmeijer, D. A. Pijnappels, M. C. Bolling, P. van der Meer, A. W. Feinberg, Dynamic loading of human engineered heart tissue enhances contractile function and drives a desmosome-linked disease phenotype, *Sci. Transl. Med.* **13**, eabd1817 (2021).

42. F. Faul, E. Erdfelder, A. Buchner, A.-G. Lang, Statistical power analyses using G*Power 3.1: tests for correlation and regression analyses, *Behav. Res. Methods* **41**, 1149–1160 (2009).

43. O. H. Cingolani, D. A. Kass, Pressure-volume relation analysis of mouse ventricular function, *Am. J. Physiol. Heart Circ. Physiol.* **301**, H2198-2206 (2011).

44. F. Rudolph, J. Hüttemeister, K. da Silva Lopes, R. Jüttner, L. Yu, N. Bergmann, D. Friedrich, S. Preibisch, E. Wagner, S. E. Lehnart, C. C. Gregorio, M. Gotthardt, Resolving titin's lifecycle and the spatial organization of protein turnover in mouse cardiomyocytes, *Proc. Natl. Acad. Sci. U. S. A.* **116**, 25126–25136 (2019).

45. A. Moretti, M. Bellin, A. Welling, C. B. Jung, J. T. Lam, L. Bott-Flügel, T. Dorn, A. Goedel, C. Höhnke, F. Hofmann, M. Seyfarth, D. Sinnecker, A. Schömig, K.-L. Laugwitz, Patient-specific induced pluripotent stem-cell models for long-QT syndrome, *N. Engl. J. Med.* **363**, 1397–1409 (2010).

46. K. Breckwoldt, D. Letuffe-Brenière, I. Mannhardt, T. Schulze, B. Ulmer, T. Werner, A. Benzin, B. Klampe, M. C. Reinsch, S. Laufer, A. Shibamiya, M. Prondzynski, G. Mearini, D. Schade, S. Fuchs, C. Neuber, E. Krämer, U. Saleem, M. L. Schulze, M. L. Rodriguez, T. Eschenhagen, A. Hansen, Differentiation of cardiomyocytes and generation of human engineered heart tissue, *Nat. Protoc.* **12**, 1177–1197 (2017).

47. S. Frank, M. Zhang, H. R. Schöler, B. Greber, Small molecule-assisted, line-independent maintenance of human pluripotent stem cells in defined conditions, *PloS One* **7**, e41958 (2012).

48. Y. Psaras, F. Margara, M. Cicconet, A. J. Sparrow, G. G. Repetti, M. Schmid, V. Steeples, J. A. L. Wilcox, A. Bueno-Orovio, C. S. Redwood, H. C. Watkins, P. Robinson, B. Rodriguez, J. G. Seidman, C. E. Seidman, C. N. Toepfer, CalTrack: High-Throughput Automated Calcium Transient Analysis in Cardiomyocytes, *Circ. Res.* **129**, 326–341 (2021).

49. I. Mannhardt, U. Saleem, A. Benzin, T. Schulze, B. Klampe, T. Eschenhagen, A. Hansen, Automated Contraction Analysis of Human Engineered Heart Tissue for Cardiac Drug Safety Screening, *J. Vis. Exp. JoVE* **122** (2017), doi:10.3791/55461.

50. C. M. Warren, P. R. Krzesinski, M. L. Greaser, Vertical agarose gel electrophoresis and electroblotting of high-molecular-weight proteins, *Electrophoresis* **24**, 1695–1702 (2003).

51. Y. I. Li, D. A. Knowles, J. Humphrey, A. N. Barbeira, S. P. Dickinson, H. K. Im, J. K. Pritchard, Annotation-free quantification of RNA splicing using LeafCutter, *Nat. Genet.* **50**, 151–158 (2018).

52. D. Garrido-Martín, E. Palumbo, R. Guigó, A. Breschi, ggsashimi: Sashimi plot revised for browser- and annotation-independent splicing visualization, *PLoS Comput. Biol.* **14**, e1006360 (2018).

53. M. Pertea, G. M. Pertea, C. M. Antonescu, T.-C. Chang, J. T. Mendell, S. L. Salzberg, StringTie enables improved reconstruction of a transcriptome from RNA-seq reads, *Nat. Biotechnol.* **33**, 290–295 (2015).

54. Britto-Borges, Thiago, *Source code to produce the PSI plots* (Zenodo, 2021; https://zenodo.org/record/5544014).

55. M. H. Radke, C. Polack, M. Methawasin, C. Fink, H. L. Granzier, M. Gotthardt, Deleting Full Length Titin Versus the Titin M-Band Region Leads to Differential Mechanosignaling and Cardiac Phenotypes, *Circulation* **139**, 1813–1827 (2019).

Acknowledgments:

We thank Carmen Judis, Janine Fröhlich and Andra Eisenmann for expert technical assistance. We are grateful to the animal phenotyping facility (MDC) for the ECG, echocardiography, and catheter measurements (Martin Taube, Stefanie Schelenz, Astrid Schiche, Alina El-Khalili, Arnd Heuser) and to Alessandra Moretti and Sebastian Diecke from the MDC/BIH stem cell core facility for access to iPSCs / iPSC-CM. **Funding**: This work was supported by The Deutsche Forschungsgemeinschaft, Bonn, Germany (MG); Deutsches Zentrum für Herz-Kreislaufforschung (MG, CD, TBB); The European Research Council grant StG282078 (MG); and the Bundesministerium für Bildung und Forschung, Berlin, Germany (CaRNAtion, MG). The work of CD and TBB was kindly supported by the Klaus Tschira Stiftung gGmbH (grant 00.219.2013).

Author contributions: D.K. performed the ASO screening. M.H.R. and D.K. performed the animal experiments, V.B.-L., R.J., D.K., P.P. performed the cell culture experiments, M.H.R., V.B.-L. and J.H. performed the microscopy analysis, M.H.R., V.B-L. and M.L. performed the molecular experiments. M.H.R., V.B-L., R.J., P.P, J.L.C., J.H., D.K., M.L., C.D., and M.G. analyzed and visualized data. T.B.-B. and C.D. analyzed and visualized transcriptomics data. A.H. provided crucial reagents and supported the analysis of EHT data. M.H.R., V.B.-L., A.M. and M.G. contributed to experimental design and supervision of the project, M.G. conceived the project and wrote the manuscript with input from all authors. **Competing interests**: A.M. and D.K. are employees of Ionis Pharmaceuticals, Inc.

Data and materials availability: All data associated with this study are present in the paper or the Supplementary Materials. Animals and reagents are available upon reasonable request following institutional guidelines (material transfer agreement through the corresponding author). RNAseq data have been deposited in the ArrayExpress database at EMBL-EBI (www.ebi.ac.uk/arrayexpress) under accession number E-MTAB-9361.

Figures:

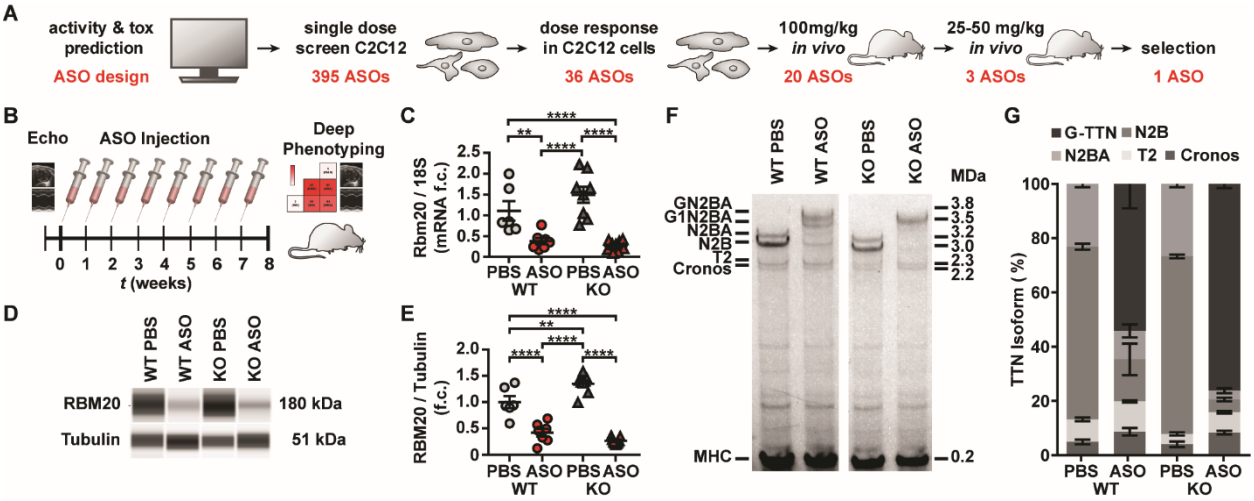

Fig. 1. **Injection of RBM20 ASO efficiently suppresses cardiac RBM20 expression and titin exon skipping in mice. (A)** Workflow to identify ASOs directed against murine RBM20 in silico, in C2C12 cells, and in vivo. Number of candidates in red. **(B)** Experimental design for in vivo work. **(C)** *Rbm20* mRNA in heart tissue from wildtype (WT) and N2B knockout mice (KO) treated with PBS or ASO. **(D, E)** Corresponding RBM20 protein abundance compared to the housekeeper tubulin in WES. **(F)** Vertical agarose gel analysis of titin isoform expression. The mature N2BA and N2B shift to the giant N2BA isoforms after ASO treatment. **(G)** Quantification of titin isoforms in (F). G -TTN, giant titin isoform. WT PBS n = 6; WT ASO n = 7; KO PBS n = 8, KO ASO n = 9. Data shown as mean ± SEM. Two-Way ANOVA with Tukey´s multiple comparison post-test, $^{**}P < 0.01$, $^{****}P < 0.0001$.

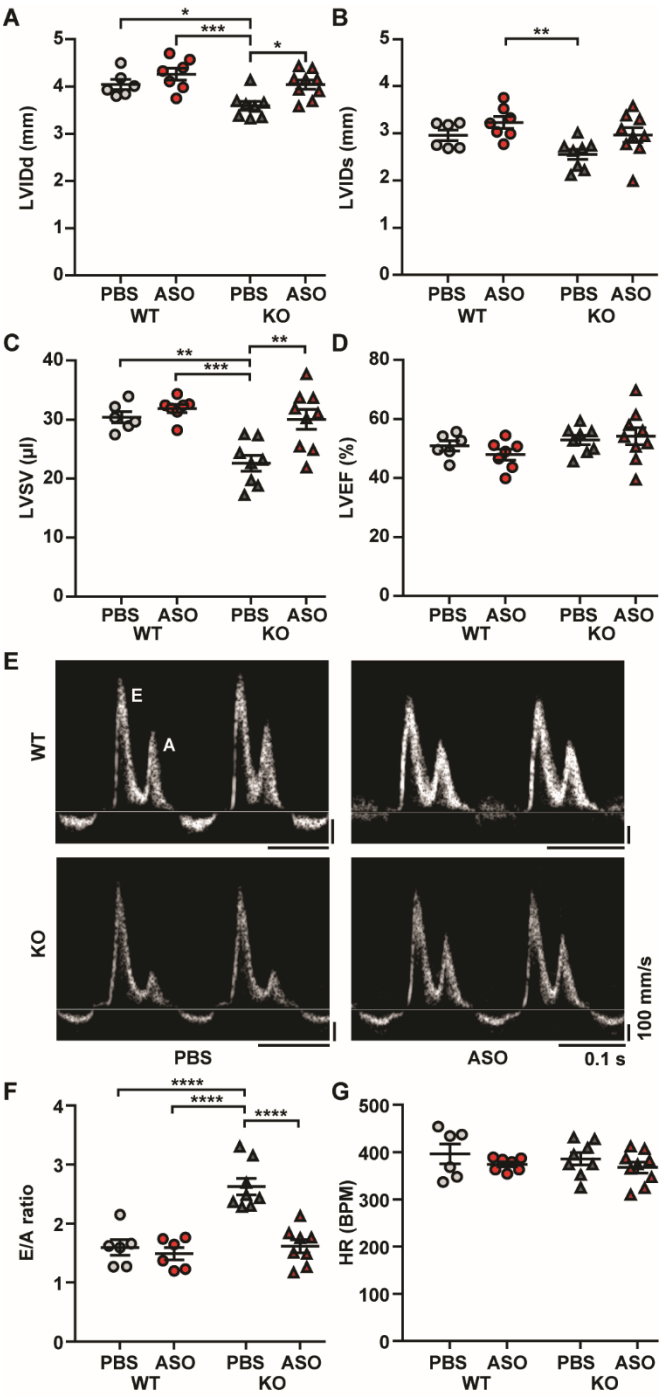

Fig. 2. **Left ventricular dimensions and diastolic function are restored in titin N2B knockout (KO) hearts after 8 weeks of RBM20 ASO treatment.** Left ventricular inner diameter in diastole (LVIDd, **A**), systole (LVIDs, **B**), stroke volume (LVSV, **C**), and ejection fraction (LVEF, **D)** in WT and KO mice treated with PBS or ASO. **(E)** Doppler analysis of mitral inflow with the E/A ratio as a parameter of diastolic function between groups. **(F)** E/A ratio and **(G)** heart rate (HR) in WT and KO mice after PBS or ASO treatment. WT PBS n = 6; WT ASO n = 7; KO PBS n = 8 and KO ASO n = 9. Data

shown as mean ± SEM. Two-Way ANOVA with Tukey´s multiple comparison post-test, *$P < 0.05$, **$P < 0.01$, ***$P < 0.001$, ****$P < 0.0001$. BPM, beats per minute.

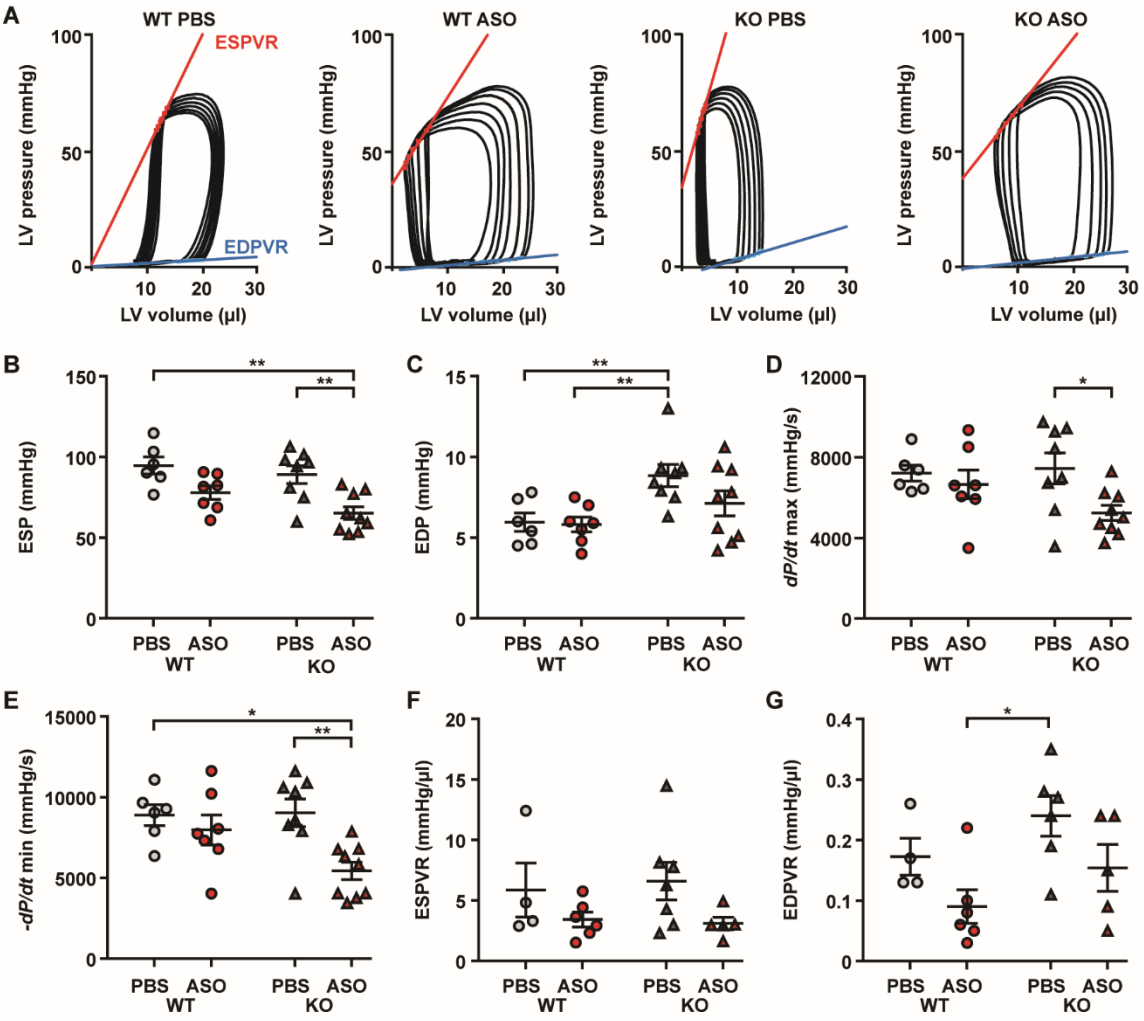

Fig. 3. Pressure-volume relations in N2B KO hearts are normalized after RBM20 ASO treatment. (A) Pressure-volume (PV) loops of WT and KO mice treated with PBS vs. RBM20 ASO. End-systolic and end-diastolic pressure-volume relationships (ESPVR, red; EDPVR, blue) serve as a measure of end-systolic elastance and diastolic stiffness, respectively. **(B)** End-systolic pressure (ESP), **(C)** end diastolic pressure (EDP), maximum velocity of contraction (dP/dt max, **D**) and relaxation (-dP/dt min, **E**), (**F**) ESPVR, and (**G**) EDPVR in WT and KO mice after PBS or ASO treatment for 8 weeks. WT PBS control n = 6; WT ASO n = 7; KO PBS control n = 8 and KO ASO n = 9 (ESPVR and EDPVR data could not be analyzed in all animals). Data shown as mean ± SEM. Two-way ANOVA with Tukey´s multiple comparison post-test, *$P < 0.05$, **$P < 0.01$.

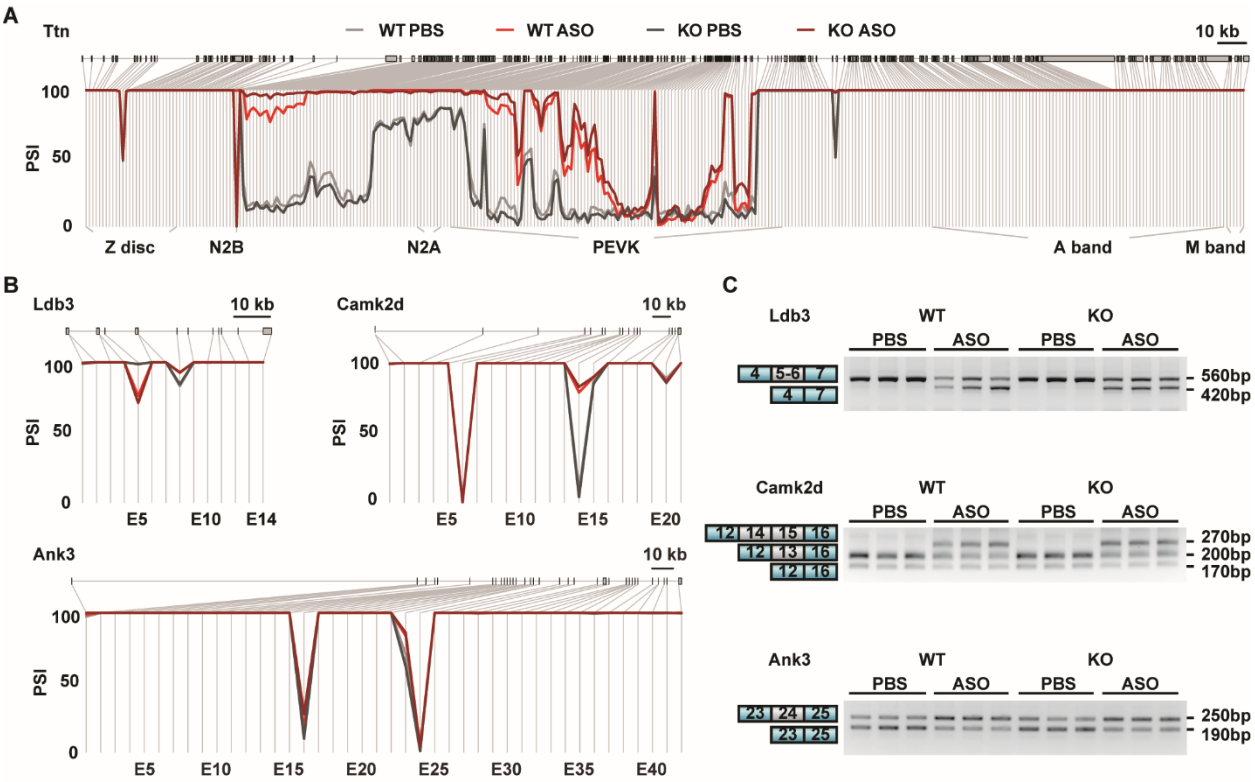

Fig. 4. RBM20 ASOs modify cardiac isoform expression. Transcriptomic analysis of cardiac splicing after 8 weeks of ASO treatment in WT and KO mice. **(A)** Percent spliced in (PSI) values for titin exons. **(B)** Splicing in the RBM20 targets *Ldb3*, *Camk2d* and *Ank3*. **(C)** Validation of ASO-dependent splicing by RT-PCR. Spliced exons are indicated on the left, PCR product size on the right. RNAseq n = 4 per group, RT-PCR n = 3 per group. bp, base pair.

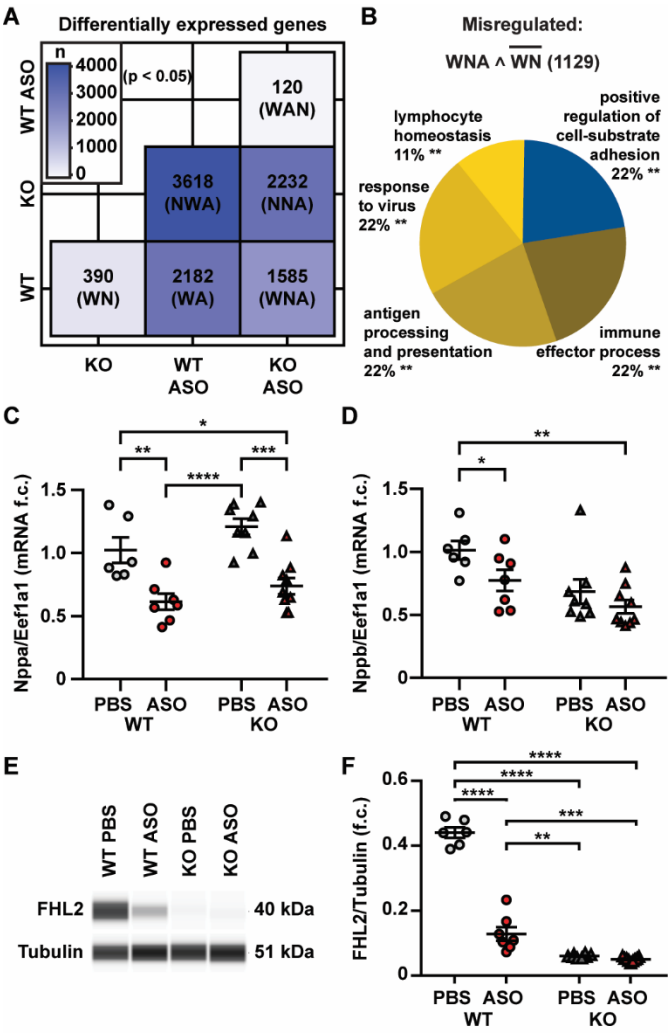

Fig. 5. ASO treatment induces expression of genes related to the immune response and suppresses titin binding protein FHL2. (A), Changes in gene expression between WT and KO with and without ASO treatment. The ASO-effect is >5 times stronger than the genotype effect. **(B)** Gene ontology analysis of genes misregulated after ASO treatment. Genes regulated in KO with ASO but not in KO PBS relate to the immune response (shades of yellow) and cell-matrix interactions (blue). **(C,D)** mRNA expression of the hypertrophy markers natriuretic peptide A (*Nppa*) and natriuretic peptide B (*Nppb*) after RBM20 ASO treatment. **(E)** Protein expression of the titin binding protein FHL2 after ASO treatment in the WT and KO groups. **(F)** Quantification of the FHL2 WES in (E). n = 4 animals per group for RNAseq analysis; WT PBS n = 6; WT ASO n = 7; KO PBS control n = 8 and KO ASO n = 9 animals for mRNA and protein analyses. Data shown as mean ± SEM. Two-way ANOVA with Tukey´s multiple comparison post-test, **P* < 0.05, ***P* < 0.01, ****P* < 0.001, *****P* < 0.0001. f.c., fold change.

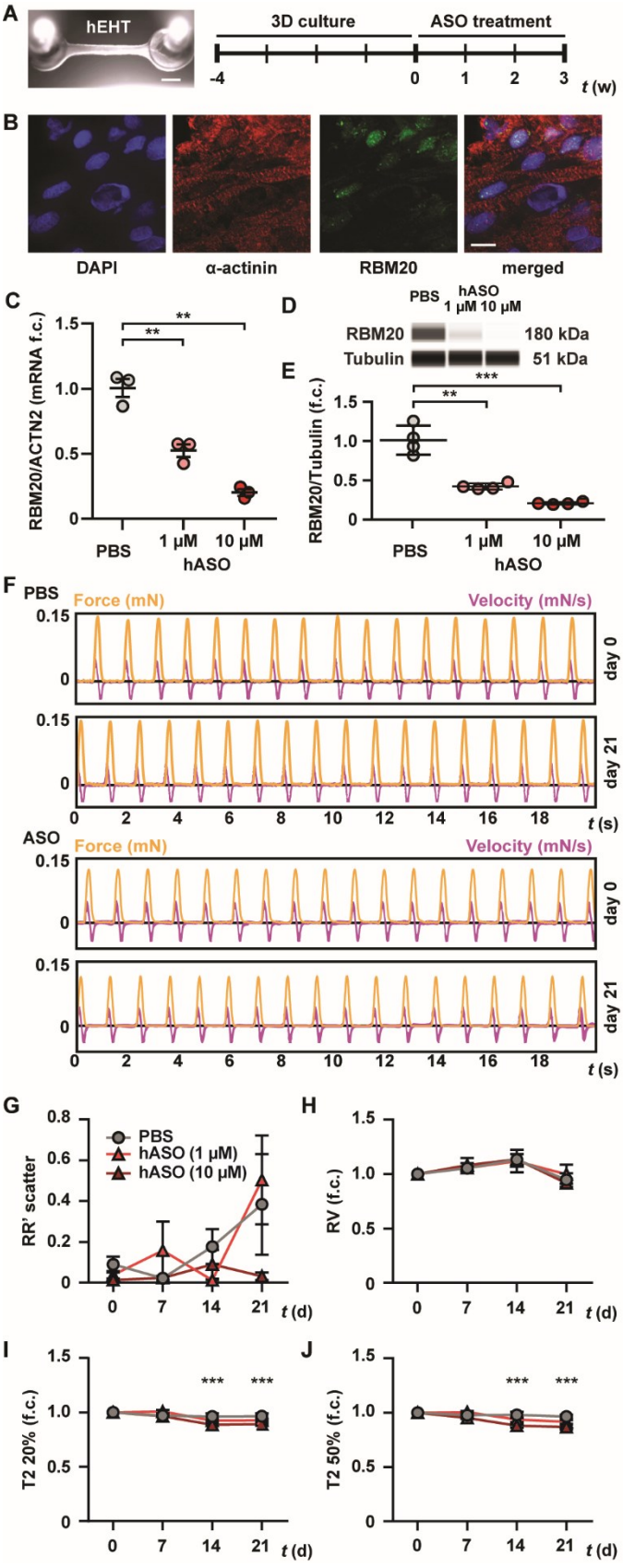
A
hEHT
3D culture
ASO treatment
-4
0
1
2
3
t (w)
B
DAPI
α-actinin
RBM20
merged
C
RBM20/ACTN2 (mRNA f.c.)
PBS
1 μM
10 μM
hASO
D
PBS
hASO
1 μM 10 μM
RBM20
180 kDa
Tubulin
51 kDa
E
RBM20/Tubulin (f.c.)
F
PBS
Force (mN)
Velocity (mN/s)
day 0
day 21
t (s)
ASO
G
RR² scatter
PBS
hASO (1 μM)
hASO (10 μM)
t (d)
H
RV (f.c.)
I
T2 20% (f.c.)
J
T2 50% (f.c.)

Fig. 6. ASO-mediated downregulation of RBM20 in human engineered heart tissue (hEHT). (A) Photo micrograph of hEHT and timeline of generation and treatment with RBM20 ASO in weeks. Scale bar = 1 mm. **(B)** Immunofluorescence analysis of RBM20 nuclear localization in hiPSC-CM within the EHT. Scale bar = 10 µm. **(C)** *RBM20* mRNA expression after 21 days of ASO-treatment (qRT-PCR). **(D)** Expression of RBM20 protein and tubulin (loading control) determined by WES. **(E)** Quantification of protein expression in (D). **(F)** Representative force and velocity curves of hEHT contraction before and after ASO treatment. **(G)** RR' scatter over time in culture with ASO treatment. **(H)** Relaxation velocity (RV) over time between groups. **(I)** $T2_{20\%}$ and **(J)** $T2_{50\%}$ after ASO treatment. n = 4 per group. One cardiomyocyte differentiation batch was used for EHT generation. Data shown as mean ± SEM. One-way ANOVA with Tukey´s multiple comparison post-test **(C,E)**; Two-way ANOVA with Dunnett's post-test **(G-J)**, $^{**}P < 0.01$, $^{***}P < 0.001$. f.c., fold change.

Supplementary Material

Supplementary Figures

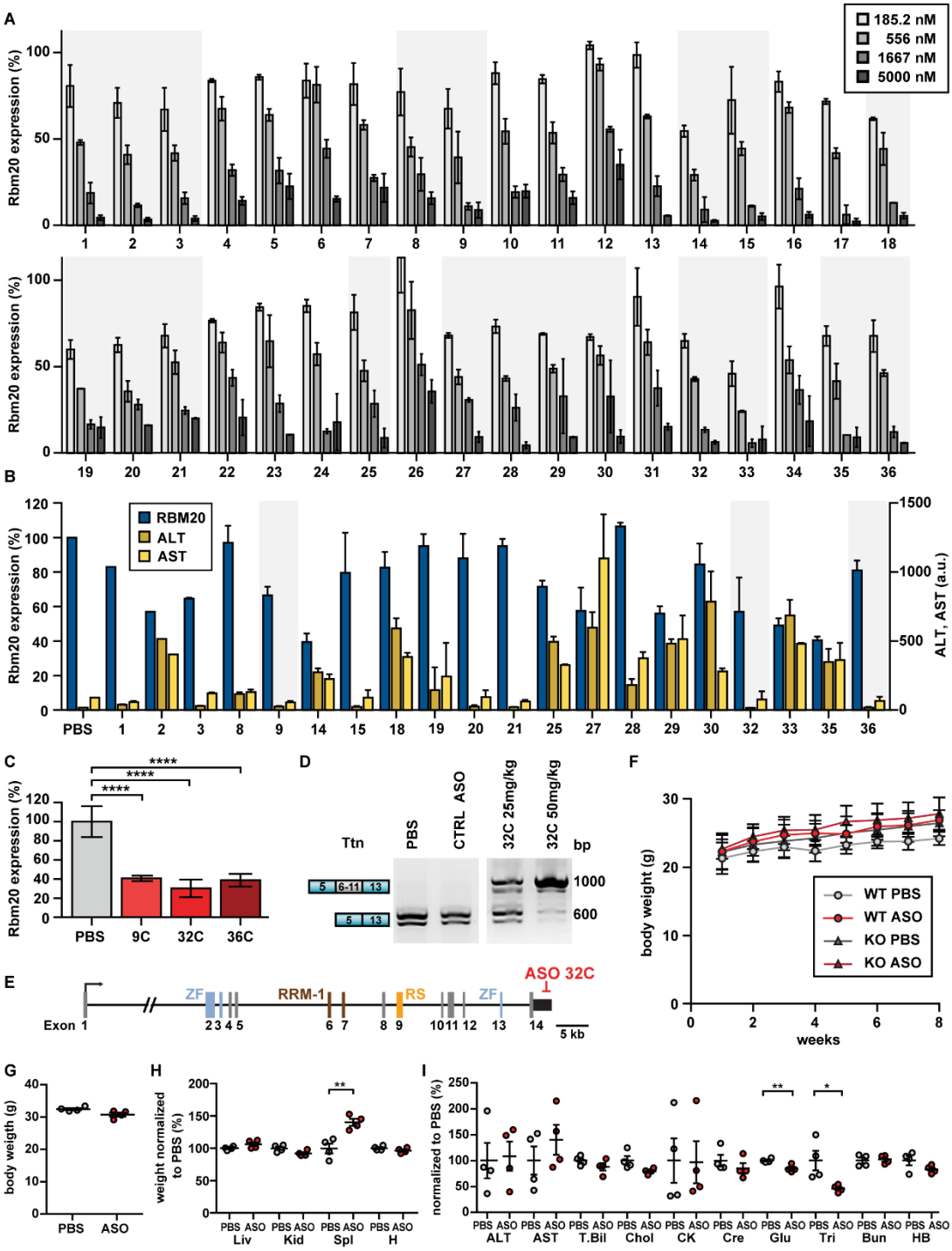

Fig. S1. Screening and selection of RBM20 ASOs in vitro and in vivo. (A) RBM20 ASO dose response in C2C12 myoblasts as determined by RT-PCR of Rbm20 (185.2 nM to 5 µM). The most efficient ASOs downregulated Rbm20 to < 50% at the lowest concentration and < 10% at the highest concentration. **(B)** In vivo RT-PCR analysis of the top 20

candidates after injecting mice with 100 mg / kg / w for 3 weeks. Cardiac Rbm20 expression (left y-axis) was reduced by up to > 50%, but several candidates were hepatotoxic (increased expression of ALT and AST expression-right y-axis). n = 2 animals per ASO. **(C)** Rbm20 expression in heart tissue from mice treated with ASOs at 50 mg/kg/w for 3 weeks (RT-PCR with n = 4 animals per group). One-way ANOVA with Tukey's post-test. ****$P < 0.0001$. **(D)** Cardiac titin (Ttn) splicing in relation to the concentration of 32C ASO. **(E)** Exon structure of Rbm20 with ASO target sequence (red). **(F)** Body weight curves of wildtype (WT) and Titin N2B knockout (KO) mice treated for 8 weeks with RBM20 ASO (50 mg/kg/week) or PBS. WT PBS n = 6; WT ASO n = 7; KO PBS control n = 8 and KO ASO n = 9. **(G, H)** Body- and normalized tissue weights in PBS and ASO treated wildtype mice (Liv liver; Kid kidney; Spl spleen; H heart). **(I)** Serum parameters for ALT (alanine aminotransferase), aspartate transaminase (AST), total bilirubin (T Bil), cholesterol (Chol), creatine kinase (CK), creatinine (Cre), glucose (Glu), triglycerides (Tri), blood urea nitrogen (Bun), hemoglobin (HB). n = 4 animals per group in G-I. Data shown as mean ± SEM. Unpaired t-test was used to determine statistical significance. *$P < 0.05$; **$P < 0.01$.

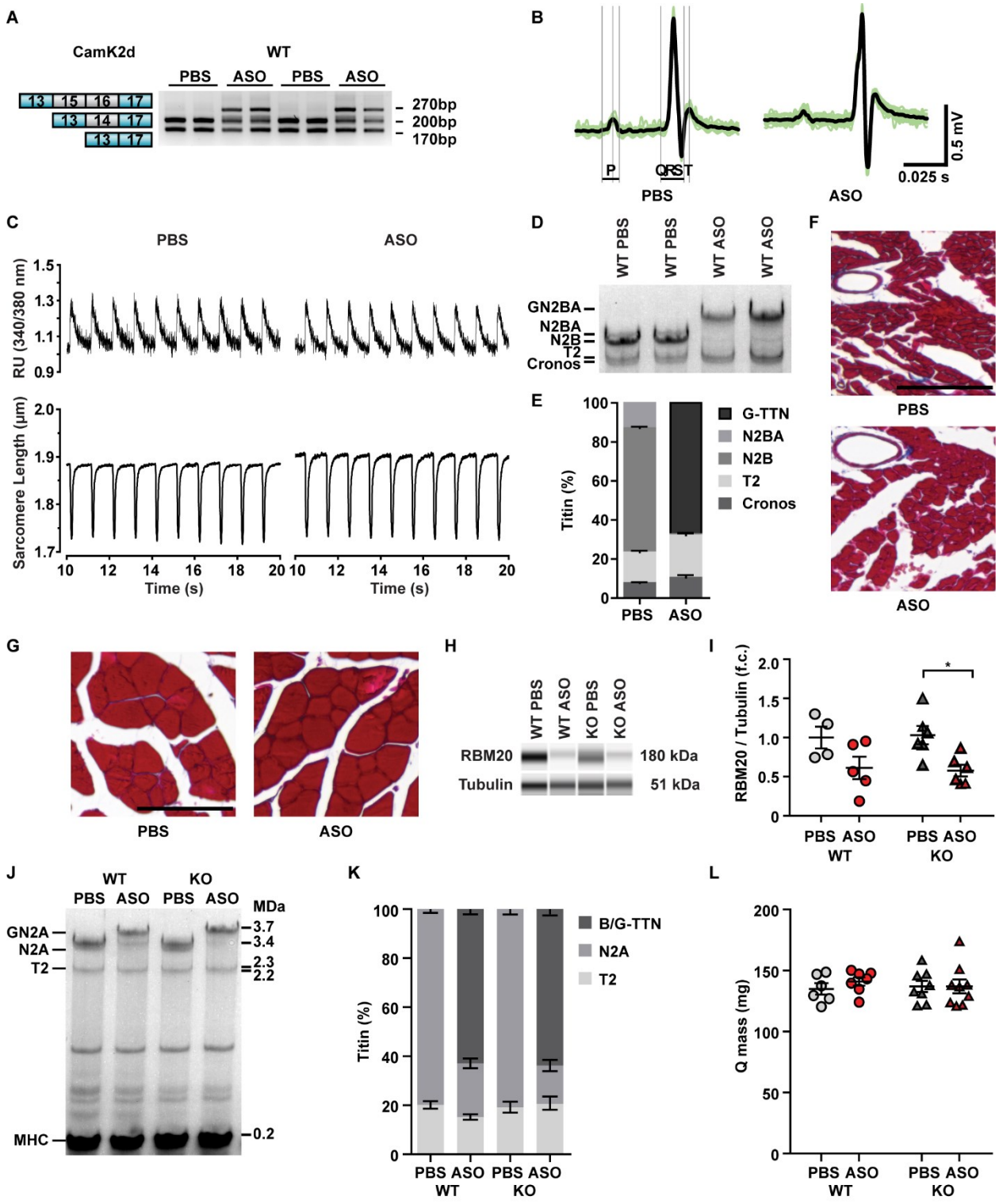

Fig. S2. Validation of RBM20 safety in heart and skeletal muscle. (A) RT-PCR of RBM20 target CAMK2D. **(B)** Representative ECG traces of RBM20 ASO-treated animals and PBS control. **(C)** Representative Ca^{2+} transients and contraction curves of primary adult mouse cardiomyocytes from 8-week RBM20 ASO-treated animals. **(D)** Shift to titin GN2BA protein isoform after RBM20 ASO treatment as determined by VAGE.

(E) Quantification of titin isoforms. **(F)** Masson's trichrome staining of heart and **(G)** skeletal muscle sections of PBS- or RBM20-treated animals. **(H)** WES of RBM20 protein expression in skeletal muscle. **(I)** Quantification of RBM20 expression in skeletal muscle. **(J)** Titin gel of wild type and knockout skeletal muscle treated with RBM20 ASO or PBS for 8 weeks. **(K)** Quantification of titin isoform expression in skeletal muscle. **(L)** Quadriceps weight in wild type and knockout mice treated with RBM20 ASO or PBS for 8 weeks. Scale bar in F and G = 100 μm. Significance was tested in I and L with two-way ANOVA followed by Tukey's multiple comparison test, Data shown as mean ± SEM. $*P < 0.05$.

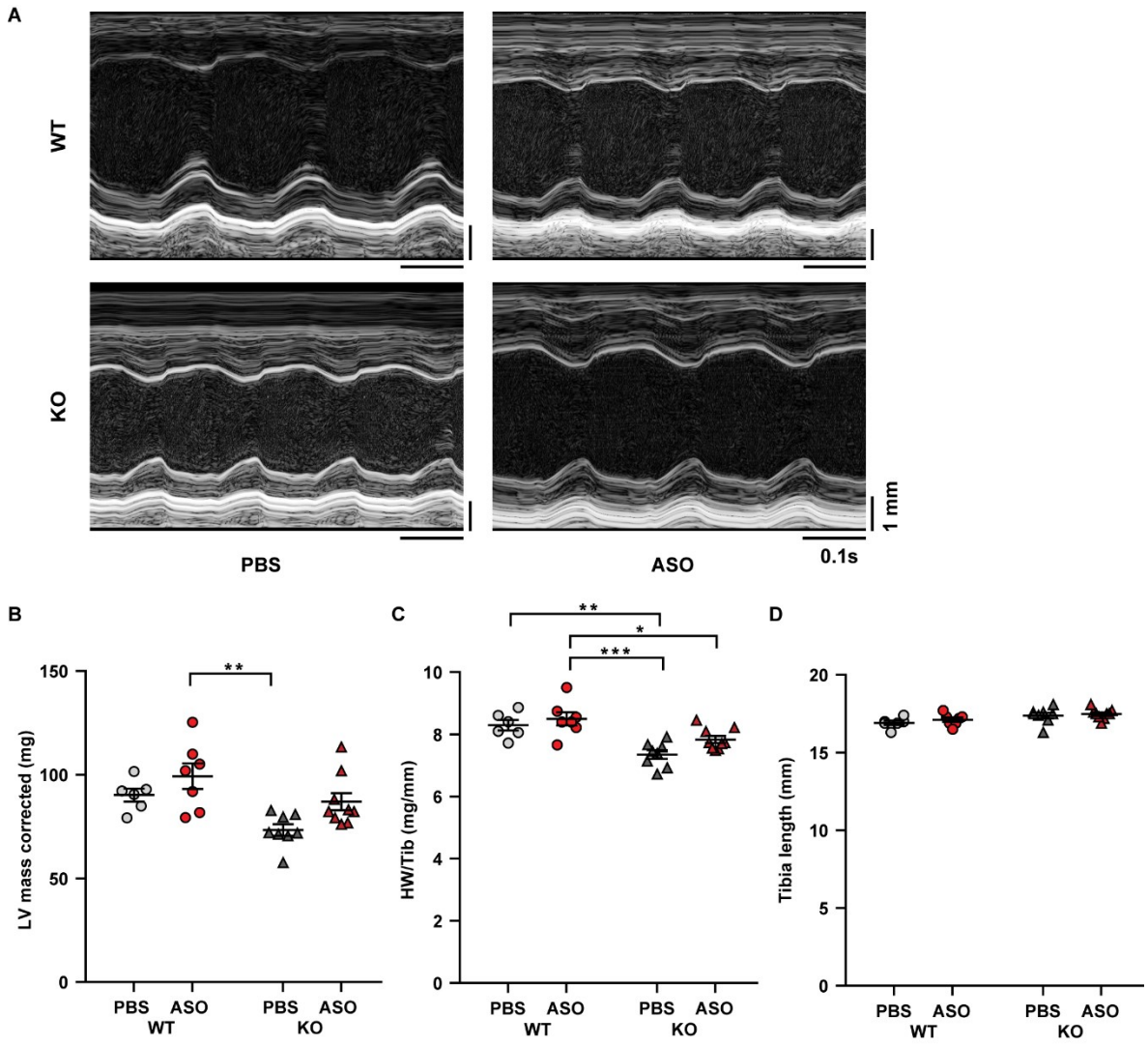

Fig. S3. Improved cardiac atrophy in titin N2B knockout (KO) mice after RBM20 ASO treatment. (A) M-mode echocardiography traces of WT and KO RBM20 treated with ASO (50 mg/kg/w) vs. PBS for 8 weeks. **(B)** Left ventricular (LV) mass calculated from echocardiography data. **(C, D)** Heart weight (HW) normalized to Tibia (Tib) length after PBS or ASO treatment. WT PBS n = 6; WT ASO n = 7; KO PBS control n = 8 and KO ASO n = 9 animals. Data shown as mean ± SEM. Two-way ANOVA with Tukey´s multiple comparison post test, **P* < 0.05, ***P* < 0.01, ****P* < 0.001.

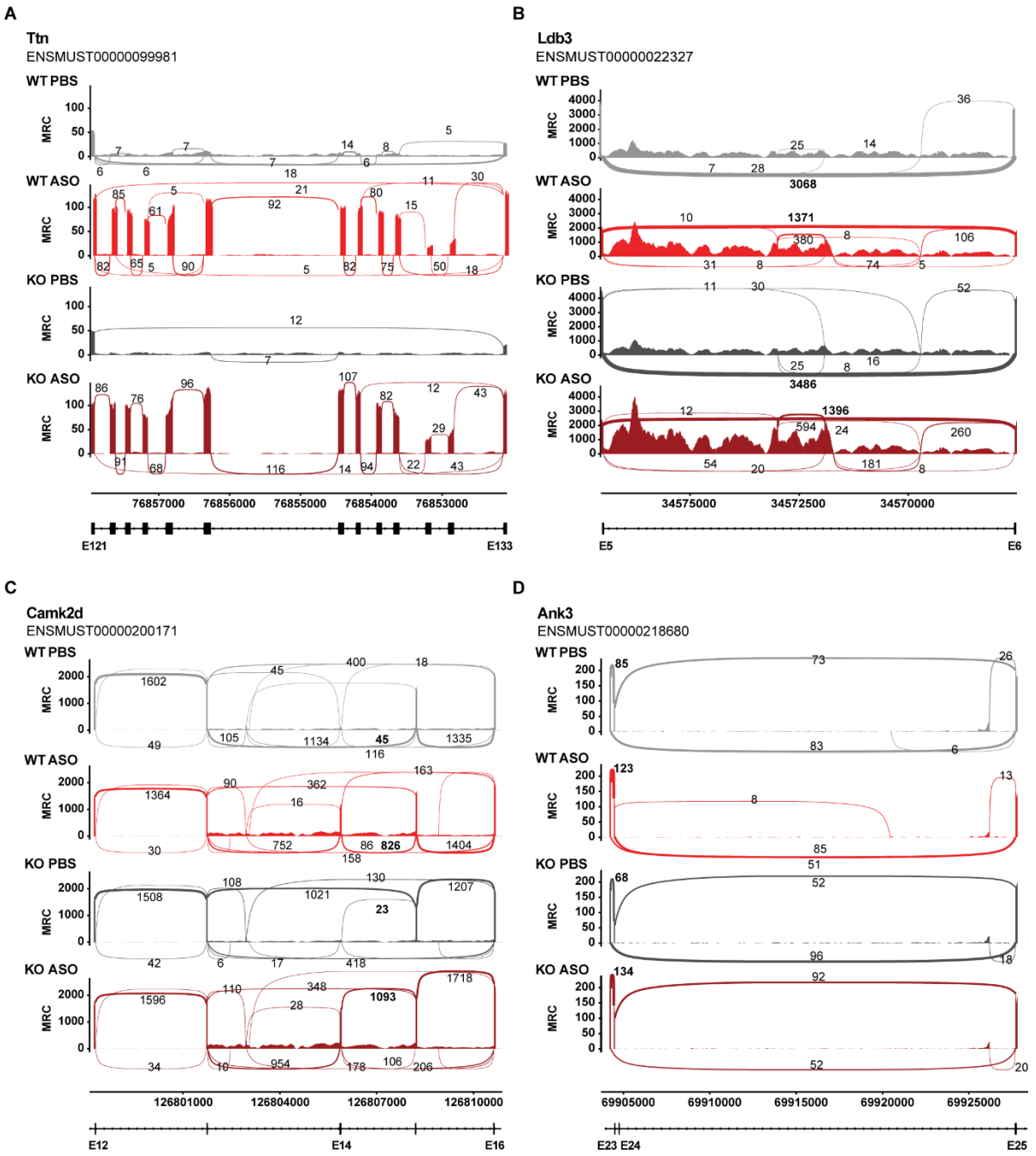

Fig. S4. ASO-dependent alternative splicing of RBM20 target genes (Sashimi Plots). Numbers of split and inclusion reads for genotype and treatment combinations. Genomic coordinates and exon numbers are provided below each set of graphs. MRC – mean read coverage **(A)** Titin exons in the PEVK region (E121 – E133) are increasingly included after ASO treatment (light and dark red). **(B)** In *Ldb3*, junction reads between Exon 5 and 6 are increased by >2-fold ASO treatment (bold). **(C)** Splicing between *Camk2d* exon 12 to 16. ASO treatment increases split reads between exon 14 and 15 (bold). **(D)** In *Ank3*, junction reads between Exon 23 and 24 are increased by >50% after ASO treatment (bold) with a matching increase in split reads between Exon 24 and 25 as compared to 23 and 25. n = 4 animals per group.

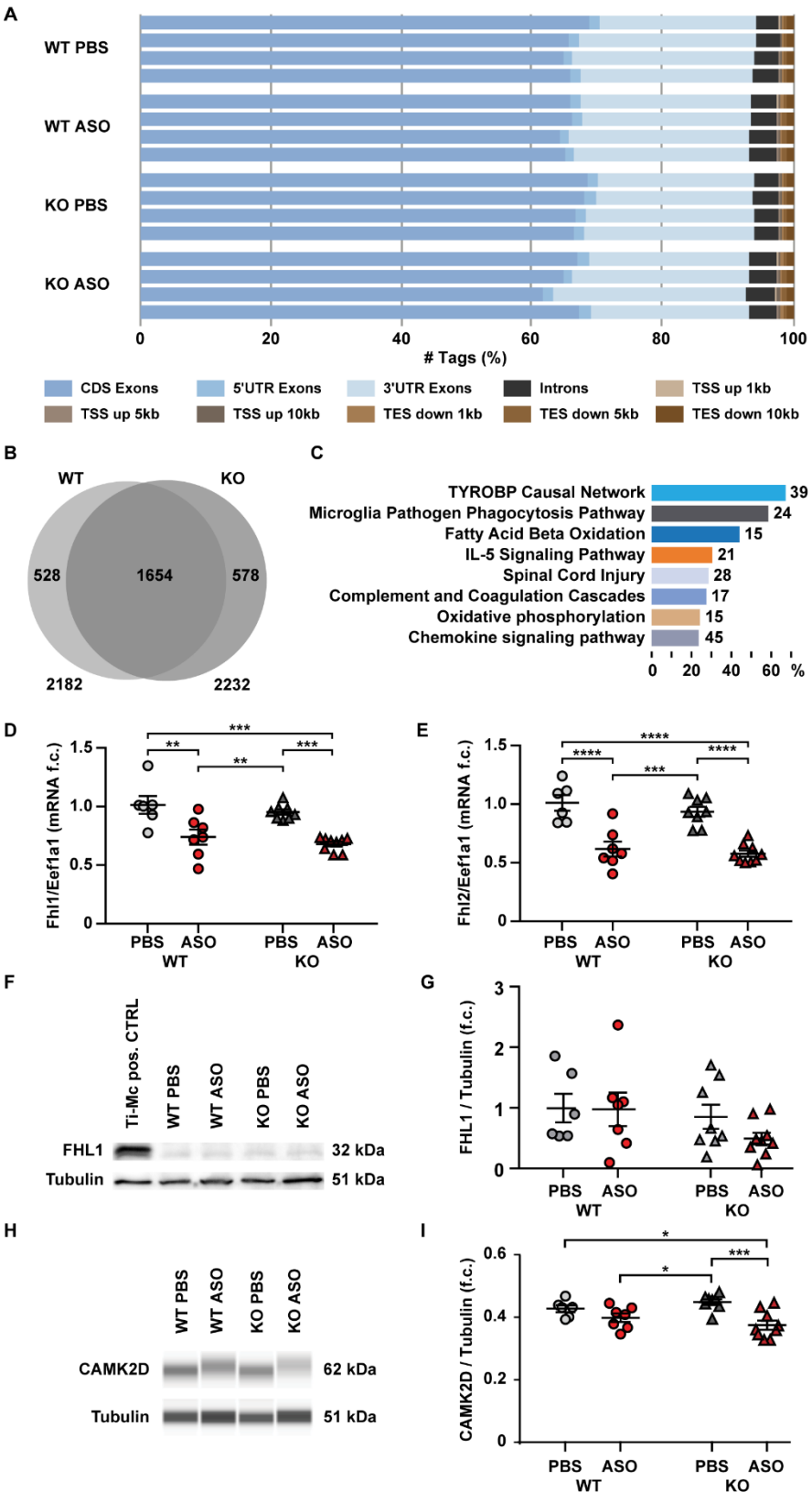

Fig. S5. RBM20 ASOs affect pathways related to immune signaling, metabolism, and growth. (A) Read alignment distribution. Reads were assigned to coding sequence

(CDS), untranslated region (UTR), and their location upstream of the transcription start sequence (TSS) or downstream of the transcription end sequence (TES). **(B)** Venn diagram of ASO-responsive gene expression in WT vs. KO hearts. More than 2000 genes were deregulated in each genotype with ~75% overlap (1645 genes). **(C)** Wikipathway analysis of RBM20 ASO-regulated genes with Cytoscape ClueGO. Bars indicate percentage of genes and total number is to the right of each column. Pathways affected by ASO treatment relate to the immune system and metabolism, including 39 genes in the Transmembrane Immune Signaling Adaptor Network (TYRPBP). **(D)** qRT-PCR quantification of mRNA transcripts encoding the titin binding protein *Fhl1* after ASO treatment. **(E)** mRNA expression of the titin adaptor *Fhl2*. **(F)** Western blot of FHL1. **(G)** FHL1 expression in all groups. **(H)** WES of CAMK2D with reduced mobility reflecting larger isoforms after ASO treatment. **(I)** Protein abundance after RBM20 ASO treatment in (H). WT PBS n = 6; WT ASO n = 7; KO PBS control n = 8 and KO ASO n = 9 animals. Data shown as mean ± SEM. Two-way ANOVA with Tukey´s multiple comparison post test, *$P < 0.05$, **$P < 0.01$, ***$P < 0.001$, ****$P < 0.0001$.

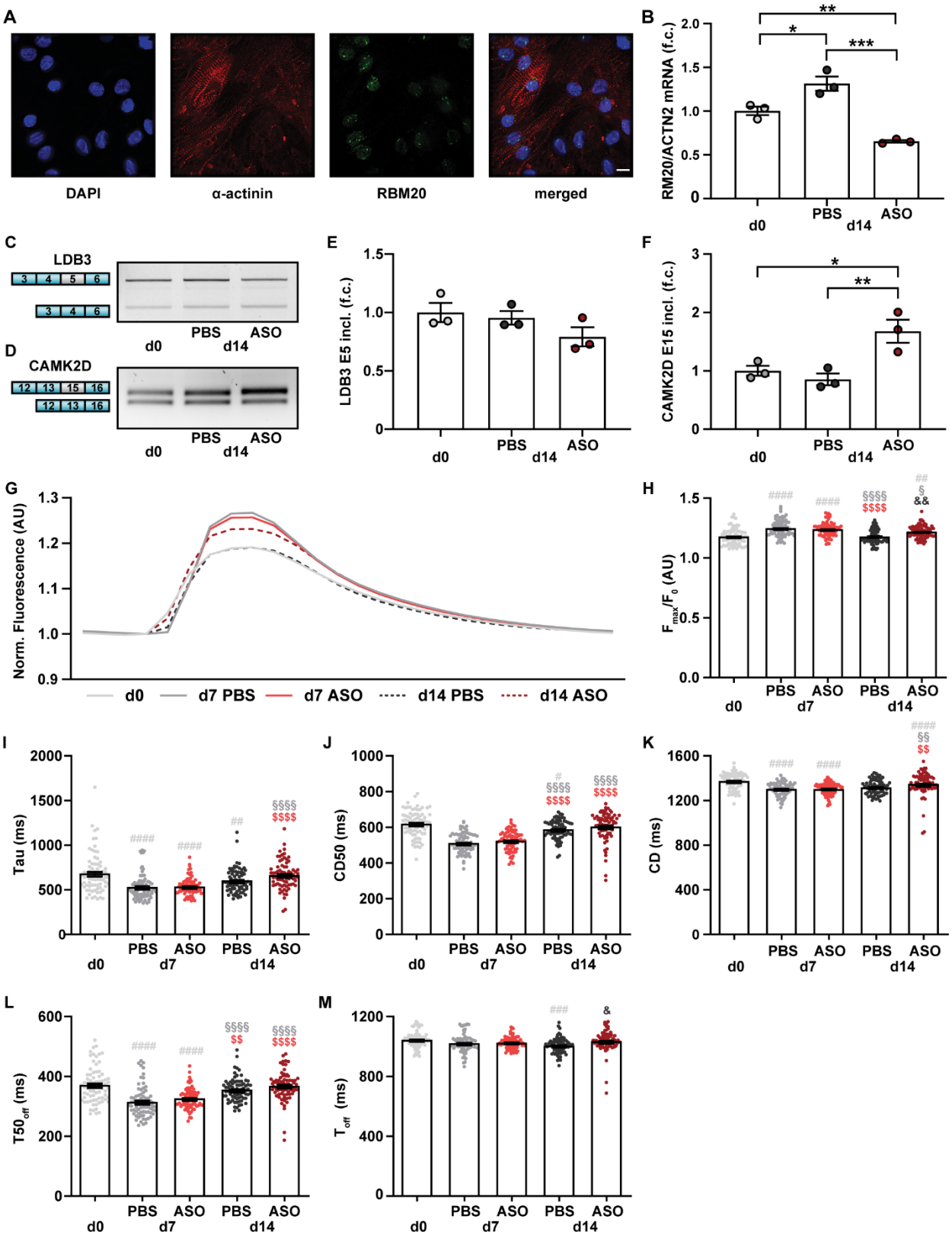
A
DAPI
α-actinin
RBM20
merged
B
RM20/ACTN2 mRNA (f.c.)
d0
PBS
ASO
d14
C
LDB3
D
CAMK2D
E
LDB3 E5 incl. (f.c.)
F
CAMK2D E15 incl. (f.c.)
G
Norm. Fluorescence (AU)
d0
d7 PBS
d7 ASO
d14 PBS
d14 ASO
H
F_max/F_0 (AU)
d7
I
Tau (ms)
J
CD50 (ms)
K
CD (ms)
L
T50_off (ms)
M
T_off (ms)

Fig. S6. **Calcium imaging in paced hiPSC-derived cardiomyocytes. (A)** RBM20 localization in the nucleus. Size-bar = 10 µm. **(B)** *RBM20* expression after 14 days of treatment with 1 µM ASO (qRT-PCR). **(C)** *LDB3* splicing as determined by RT-PCR of exons 3-6. **(D)** *CAMK2D* isoform shift as determined by RT-PCR of exons 12-16. **(E, F)** Densitometry of the *LDB3* and *CAMK2D*, respectively. Upper-to-lower band intensity ratio related to the baseline average (day 0) with increased inclusion of *CAMK2D* exon 15 after 14 days of ASO treatment. **(G)** Average calcium transients of cardiomyocytes at baseline (day 0), day 7 and day 14 of control (PBS) and 1 µM ASO treatment. **(H)** Peak fluorescence normalized to baseline (F_{max}/F_0) after 14 days of ASO treatment. **(I-L)** The calcium decay constant (Tau), 50% transient duration (CD50), transient duration (CD) and time of 50% calcium decay ($T50_{off}$) compared to the time-matched controls. **(M)** The length of calcium decay (T_{off}) after ASO treatment. **(B, E, F)** n= 3 for qRT- and RT-PCR. Data shown as mean ± SEM. Two-way ANOVA with Tukey's multiple comparison test. Asterisks indicate difference between treatments, **P* < 0.05; ***P* < 0.01, *****P* < 0.0001. **(H-M)** n = 75 cells per group for calcium imaging. One cardiomyocyte differentiation batch was used for calcium imaging. Two-way ANOVA with Tukey's multiple comparison test: significant between groups # compared to day 0, § compared to day 7 PBS, $ compared to day 7 ASO, & compared to day 14 PBS. **P* < 0.05; ***P* < 0.01; ****P* < 0.001 *****P* < 0.0001 versus respective group.

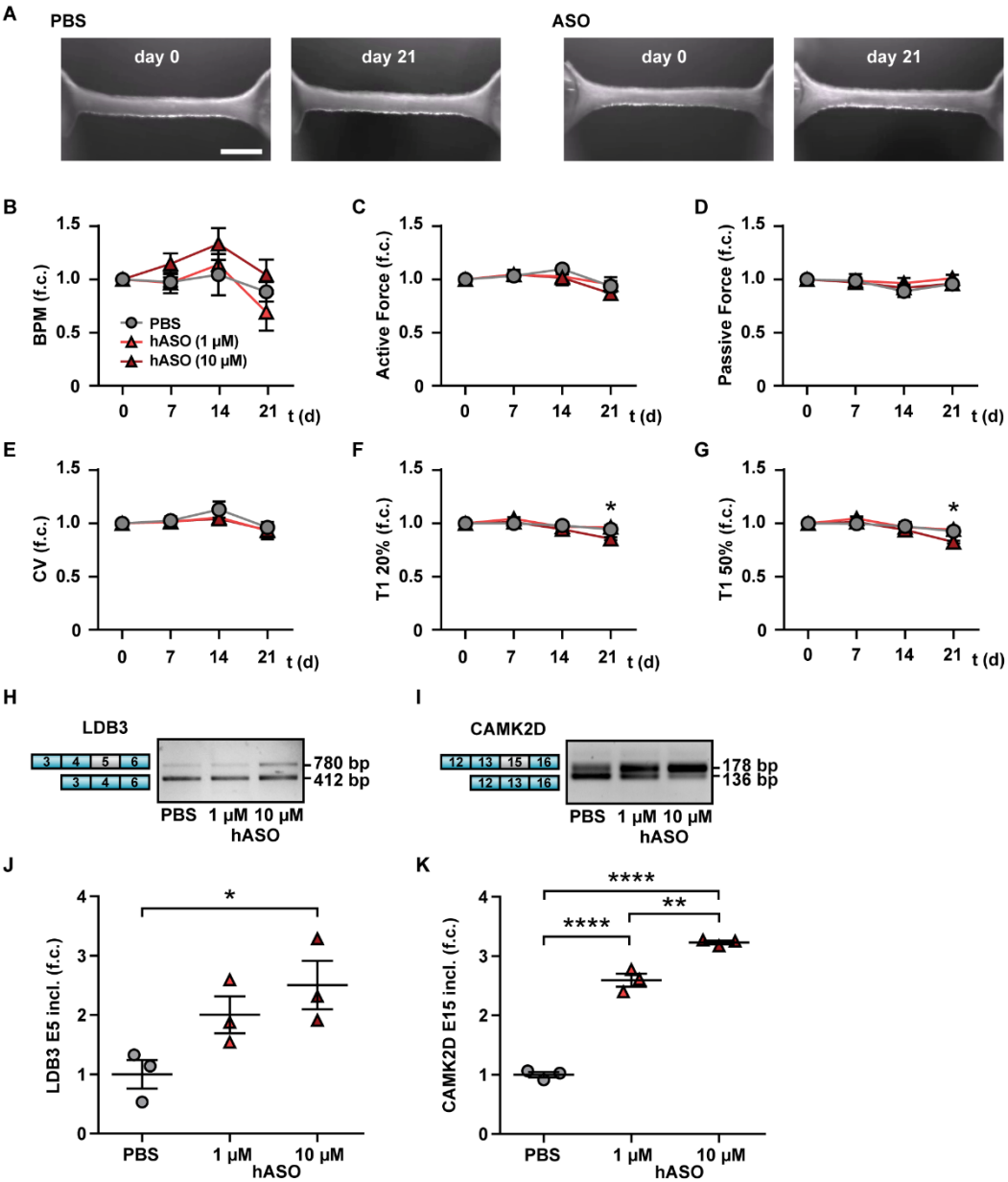

Fig. S7. RBM20 ASOs increase exon inclusion of RBM20 targets with minor effects on contraction velocities. (A) Morphology of PBS and ASO treated hEHTs. Scale bar = 1 mm. **(B-D)** Beating rate per minute (BPM), active-, and passive force according to treatment. **(E-G)** Contractile parameters of EHTs over 21 days of treatment. CV = contraction velocity, T1= contraction time. **(H, I)** *LDB3* and *CAMK2D* isoform shift as determined by RT-PCR of exons 3-6 and 12-16, respectively; **(J,K)** RT-PCR gel densitometry of the differentially included *LDB3* and *CAMK2D* exons (upper band normalized to the combined upper and lower band intensity). **(B-G)** n = 4 h EHTs per treatment. Data shown as mean ± SEM. Two-way ANOVA with Dunnett's multiple comparison test. **(H-K)** n = 3 h EHTs per treatment. One cardiomyocyte differentiation batch was used for EHT generation. One-way ANOVA with Tukey's multiple comparison test. Asterisks indicate difference between treatments, *$P < 0.05$; **$P < 0.01$, ****$P < 0.0001$.

Supplementary Tables

Table S1. ECG of WT mice treated with PBS control vs. 8 weeks of RBM20 ASO treatment

	WT-PBS	**WT-ASO**
N	6	6
age (weeks)	16	16
ECG		
Sinus Rhythm	yes	yes
RR Interval (ms)	142.9 ± 3.8	135.9 ± 4.4
HR (bpm)	421.5 ± 11.5	443.6 ± 13.4
PR Interval (ms)	39.4 ± 0.8	37.6 ± 0.7
P Duration (ms)	11.5 ± 0.7	11.4 ± 0.7
QRS Duration (ms)	13.9 ± 0.4	13.1 ± 0.6
QT (ms)	28.6 ± 0.7	32.4 ± 2.5
QT (bazett corrected) (ms)	76.2 ± 2.1	86.7 ± 7.4

No significant difference between WT PBS and WT RBM20 ASO groups analyzed with Student's t-test.

Table S2. Contraction and Ca^{2+} measurement of adult murine cardiomyocytes after 8 week of RBM20 ASO treatment vs. PBS control

	WT-PBS	**WT-ASO**
N	4	4
age (w)	16	16
Sarcomere		
Sarcomere length (µm)	1.883 ± 0.013 (141)	1.963 ± 0.013 * (179)
Sarcomere shortening (%)	4.937 ± 0.684 (142)	4.685 ± 0.507 (179)
Contraction velocity (µm/s)	-2.352 ± 0.473 (141)	-2.317 ± 0.383 (179)
Relaxation velocity (µm/s)	1.594 ± 0.378 (140)	1.483 ± 0.251 (176)
Time to baseline 50% (s)	0.165 ± 0.025 (138)	0.155 ± 0.019 (178)
Ca^{2+}		
Ca^{2+}-increase (%)	14.36 ± 2.63 (100)	11.57 ± 1.03 (125)
Ca^{2+}- contraction velocity (RU/s)	10.95 ± 2.62 (97)	8.99 ± 1.11 (122)
Ca^{2+}- relaxation velocity (RU/s)	-1.011 ± 0.232 (87)	-0.659 ± 0.085 (119)

RU: ratio units. Data are presented as mean ± SD (n cells) and were statistically analyzed with Mann-Whitney test after ROUT outlier test (Q=1%). *$P < 0.05$

Table S3. Titin isoform expression in the mouse heart

Treatment	TTN / MHC	G-TTN / MHC	N2BA / N2B	T2 / T1	Cronos / MHC	B-TTN % of T1
PBS	0.43±0.04	0±0	0.2±0.02	0.21±0.01	0.03±0	0±0
ASO	0.51±0.03	0.34±0.02****	n.d.	0.32±0.02**	0.05±0.01*	67.21±0.8****

Titin isoform quantification from Coomassie-stained titin gel from adult murine primary cardiomyocytes isolated after 8 weeks of RBM20 ASO treatment vs. PBS control. Data were statistically analyzed with Student's t test. *$P < 0.05$, **$P < 0.01$, ***$P < 0.001$; ****$P < 0.0001$.

Table S4. Titin isoform expression of WT and N2B KO mice after 8w of RBM20 ASO treatment

Samples / Treatment	TTN / MHC	G/B-TTN / MHC	N2BA / N2B	T2 / T1	Cronos / MHC	B-TTN (% of T1)
WT PBS	0.33±0.07	0±0	0.36±0.02	0.10±0.01	0.02±0.01	0±0
WT ASO	0.41±0.09	0.54±0.09****	1.46±0.81	0.35±0.17	0.05±0.01*	79±7****
N2B KO PBS	0.28±0.03	0±0§§§§	0.41±0.02	0.04±0.01	0.01±0§§	0±0§§§§
N2B KO ASO	0.34±0.06	0.76±0.02$^{\&\&\&\&,\$\$,++++}$	1.05±0.41	0.06±0.01	0.02±0	96±1$^{\&\&\&\&,\$\$,++++}$

Quantification of titin isoforms from Coomassie-stained titin gel. Data were analyzed with a two-way ANOVA with Tukey's multiple comparison test. * WT PBS vs WT ASO; § WT ASO vs. KO PBS; & KO PBS vs. KO ASO; $ WT ASO vs. KO ASO; + WT PBS vs. KO ASO. *P < 0.05; **P < 0.01;***P < 0.001;****P < 0.0001

Table S5. Titin isoform expression in mouse tibialis anterior muscle

Samples / Treatment	TTN/MHC	T2/T1	G-TTN /MHC	GTTN % of T1
WT PBS	0.39±0.03	0.25±0.03	0±0	0±0
WT ASO	0.4±0.03	0.72±0.1	0.25±0.02****	74.2±2.3****
N2B KO PBS	0.34±0.01	0.24±0.03	0±0§§§§	0±0§§§§
N2B KO ASO	0.34±0.04	1.78±0.65+, &	0.22±0.03++++, &&&&	80.77±2.78++++, &&&&

Quantification of titin isoforms from Coomassie-stained titin gel of murine TA muscle after 8 weeks of RBM20 ASO treatment vs PBS control. Data were analyzed with a two-way ANOVA with Tukey's multiple comparison test. *WT PBS vs WT ASO; § WT ASO vs. KO PBS; & KO PBS vs. KO ASO; $ WT ASO vs. KO ASO; + WT PBS vs. KO ASO. *$P < 0.05$; **$P < 0.01$; ***$P < 0.001$; ****$P < 0.0001$

Table S6. Echocardiography of WT and N2B KO mice treated with PBS control vs. 8 weeks of RBM20 ASO

	WT PBS	WT ASO	N2B KO PBS	N2B KO ASO
N	6	7	8	9
age (w)	17	17	17	17
body weight (g)	24.4±1.2	27.0±1.3	26.7±2.3	28.0±2.2§§
LV mass (mg)	88.9±5.7	93.6±6.5	76.8±4.8$^{\&\&}$	85.6±5.2
heart/body weight	5.8±0.5	5.4±0.3$^{\&\&\&}$	4.8±0.4$^{\#\#\#}$	4.9±0.5$^{\S\ \$}$
Echocardiography				
heart rate (bpm)	396±51	374±14	386±37	368±35
stroke volume (µl)	30.4±2.3	31.9±1.9$^{\&\&\&}$	22.6±3.8$^{\#\#}$	30±5.1^{++}
Vol dia (µl)	59.9±4.3	67.1±8$^{\&\&\&\&}$	43.2±5.4$^{\#\#\#}$	55.3±7.6$^{++\ \$\$}$
Vol sys (µl)	29.5±4	35.2±7.5$^{\&\&\&}$	20.6±3.4$^{\#}$	25.6±7$^{\$}$
LV dia (mm)	4.04±0.26	4.26±0.34$^{\&\&\&}$	3.59±0.27$^{\#}$	4.04±0.29^{+}
LV sys (mm)	2.96±0.27	3.23±0.33$^{\&\&}$	2.55±0.31	2.96±0.47
LVPW dia (mm)	0.77±0.05	0.76±0.1	0.73±0.08	0.71±0.07
LVPW sys (mm)	0.96±0.12	1±0.14	1.04±0.12	0.98±0.21
IVS dia (mm)	0.76±0.03	0.78±0.11	0.79±0.09	0.78±0.09
IVS sys (mm)	1.03±0.1	1.05±0.14	1.04±0.09	1.03±0.16
FS (%)	27±4.1	24.4±2.2	29.1±4.3	24.9±3.8
EF (%)	50.9±4.1	47.9±4.9	52.9±4.5	54.1±8.7
Mitral, Doppler				
E (mm/s)	629±80	643±90	724±84	623±98
A (mm/s)	411±114	446±48$^{\&}$	283±53	380±114
E/A ratio	1.6±0.3	1.5±0.2$^{\&\&\&\&}$	2.6±0.3$^{\#\#\#\#}$	1.6±0.3^{++++}
IVRT (ms)	18.7±4	20.8±1.6	20.2±3	21.9±3.8
IVCT (ms)	22±3.8	20±1.9	19.7±4.5	21.2±3.3
MVDT (ms)	23.9±2.2	32.3±4.8$^{**\ \&\&}$	25.8±3.1	32.4±3.8$^{\S\S\S\ ++}$
ET (ms)	46.1±7.9	47.2±6.7	48.8±4.3	48.4±6.1
E' (mm/s)	27.5±8.3	20.2±2.7	26±5.2	19.8±5.1^{+}
A' (mm/s)	23.1±6.7	17.3±2.6	16.1±3.6	16.9±5.6
E' / A'	1.2±0.3	1.2±0.2	1.5±0.2	1.2±0.3
E / E'	24±5.5	32.1±4.5*	28.4±3.7	32.6±6.5§
Cardiac Performance				
CO (ml/min)	12.1±2.3	11.9±0.7	8.8±1.9$^{\#}$	11±2.2
MPI	0.9±0.2	0.9±0.1	0.8±0.1	0.9±0.1

LV, left ventricle; Vol, volume; dia, diastole; sys, systole; LVPW, left ventricle posterior wall; IVS, interventricular septum; FS, fractional shortening; EF, ejection fraction; E, E wave velocity;

A, A wave velocity; E/A ratio, ratio of E to A wave velocities; IVRT, isovolumetric relaxation time; IVCT, isovolumetric contraction time; MVDT, mitral valve deceleration time; ET, ejection time. E', E' velocity; A', A' velocity; E' / A', ratio of E' / A' velocities; E / E', ratio of E / E' velocities; CO cardiac output; MPI myocardial performance index (Tei-index). Data were analyzed with a two-way ANOVA with Tukey's multiple comparison test: significance between groups # WT PBS vs KO PBS; * WT PBS vs WT ASO; § WT PBS vs. KO ASO; & KO PBS vs WT ASO; KO PBS vs KO ASO; $ WT ASO vs KO ASO. *$P < 0.05$; **$P < 0.01$; ***$P < 0.001$ ****$P < 0.0001$.

Table S7. Pressure-volume relationship of WT and N2B KO mice treated with PBS control vs. 8 weeks of RBM20 ASO

	WT PBS	WT ASO	N2B KO PBS	N2B KO ASO
N	6	7	8	9
age (w)	17	17	17	17
body weight (g)	24.4±1.2	27.0±1.3	26.7±2.3	28.0±2.2§§
HR (BPM)	483±34	417±49*	463±31	389±27$^{\S\S\S\ ++}$
Pressure/ Volume				
MAP (mmHg)	88.9±9.6	61.8±10.5**	73.8±15.9	58.7±10.8§§§
LVESP (mmHg)	94.7±13.2	77.9±11.2	89.1±15.7	65.2±11.9$^{\S\S\ ++}$
LVEDP (mmHg)	6±1.4	5.8±1.2$^{\&}$	8.8±2$^{\#}$	7.1±2.3
Pmax (mmHg)	102.4±9.9	88.1±9.8	95.3±14.6	75.2±9.4$^{\S\S\S\ ++}$
Pmin (mmHg)	3.4±1.3	3±1.4	4.2±1.4	3.2±1.9
Pmean (mmHg)	38.7±5.3	29.7±5$^{\&}$	39±8.3	25.9±5.4$^{\S\S\ ++}$
Pdev (mmHg)	99±9.1	85.1±9.5	91.1±14.5	72±8.8$^{\S\S\S\ ++}$
LVESV (µL)	13.5±5.8	15.8±7.2	10.8±4.7	9.1±5.7
LVEDV (µL)	26.1±9.9	37.7±13.8$^{\&\ \$}$	22.9±7.1	22.9±9.9
SV (µL)	15.8±4.3	22.8±5.2$^{\&\&\ \$\$}$	13.2±4.7	14.3±5
CO (ml/min)	7.5±1.5	9.4±1.9$^{\&\ \$\$}$	6.1±2.5	5.6±2.1
CI (ml/min/BW)	308.6±54.7	351.3±77.7$^{\$\$}$	234.2±108.1	202.7±79.2
Ea (mmHg/µL)	6.2±1.3	3.5±0.6$^{\&\&}$	7.4±2.7	5.1±1.8
TPR	12.1±2.3	6.7±1.2$^{\&}$	13.3±5.4	12±4.9
EF (%)	57.4±8.4	63.4±9.6	57.8±11.2	63.5±9.8
dP/dt max (mmHg/s)	7210±979	6651±1893	7444±2188	5234±1124+
SW (mmHg*µl)	1467±579	1826±526$^{\$\$}$	1159±561	934±403
-dP/dt min (mmHg/s)	8890±1608	7970±2443	9031±2431	5435±1625$^{\S\ ++}$
TauWeiss (ms)	6.6±0.7	6.9±1.4	7.6±1.4	8.5±1.5§
ESPVR (mmHg/µl) linear	5.9±4.4	3.4±1.5	6.6±4.1	3.1±1.2
EDPVR (mmHg/µl) linear	0.17±0.06	0.09±0.07$^{\&}$	0.3±0.19	0.15±0.09
PRSW (mmHg)	54.9±26.9	54.2±17.7	45.7±13.7	48.9±6.9

HR heart rate, MAP mean atrial pressure, LVESP left ventricle end-systolic pressure; LVEDP left ventricle end-diastolic pressure, P pressure, LVESV left ventricle end-systolic volume, LVEDV left ventricle end-diastolic volume, SV stroke volume, CO cardiac output, CI cardiac index, Ea atrial elastance, TRP total peripheral resistance, EF ejection fraction, SW stroke work, ESPVR end-systolic pressure-volume relationship, EDPVR end-diastolic pressure volume relationship, PRSW preload recruitable stroke work; Data were analyzed with a two-way ANOVA with Tukey's multiple comparison test: significant between groups # WT PBS vs KO PBS;* WT PBS vs WT ASO; § WT PBS vs. KO ASO; & KO PBS vs WT ASO; KO PBS vs KO ASO; $ WT ASO vs KO ASO. *$P < 0.05$; **$P < 0.01$; ***$P < 0.001$ ****$P < 0.0001$.

Table S8: Differentially spliced genes

WT PBS vs WT ASO	KO PBS vs N2B KO ASO	combined	shared genes
9030617O03Rik	*2610203C22Rik*	*2610203C22Rik*	*Atp2b1*
Acsl4	*3110040N11Rik*	*3110040N11Rik*	*Iqgap1*
Alpk1	*9030617O03Rik*	*9030617O03Rik*	*Dnajc13*
Anapc11	*Ank3*	*Acsl4*	*Sipa1l1*
Ank3	*Arhgap10*	*Alpk1*	*Slc38a6*
Arhgap10	*Atp2b1*	*Anapc11*	*Csnk1d*
Atp2b1	*Bod1l*	*Ank3*	*Bod1l*
Blvra	*Cadm1*	*Arhgap10*	*Cflar*
Bod1l	*Cflar*	*Atp2b1*	*Gngt2*
Cflar	*Cpsf7*	*Blvra*	*Arhgap10*
Csnk1d	*Cradd*	*Bod1l*	*Dock7*
Dnajc13	*Csnk1d*	*Cadm1*	*Slc4a7*
Dock7	*Ddhd1*	*Cflar*	*Psmg4*
Evl	*Dnajc13*	*Cpsf7*	*Tank*
Fam49b	*Dock7*	*Cradd*	*Ppcdc*
Gins1	*Elf1*	*Csnk1d*	*Gins1*
Gngt2	*Gcnt1*	*Ddhd1*	*9030617O03Rik*
H13	*Gins1*	*Dnajc13*	*Micu1*
Ighj4	*Gngt2*	*Dock7*	*Ryr2*
Iqgap1	*Inpp5b*	*Elf1*	*Mical3*
Ldb3	*Iqgap1*	*Evl*	*Ldb3*
Mapk8ip3	*Ldb3*	*Fam49b*	*Ttc17*
Mical3	*Lrch4, Gm20605*	*Gcnt1*	*Msh3*
Micu1	*Lsp1*	*Gins1*	*Ttn*
Msh3	*Madd*	*Gngt2*	*Ank3*
Myo5a	*Mical3*	*H13*	
N4bp2l1	*Micu1*	*Ighj4*	
Nsmce1	*Msh3*	*Inpp5b*	
P2ry14	*Mtx3*	*Iqgap1*	
Phldb1	*Mycbp2*	*Ldb3*	
Pitpnc1	*Nadk*	*Lrch4, Gm20605*	
Ppcdc	*Ntpcr*	*Lsp1*	
Psmg4	*Pfkfb1*	*Madd*	
Rai14	*Pnpla6*	*Mapk8ip3*	
Rcbtb2	*Ppcdc*	*Mical3*	
Ryr2	*Prkacb*	*Micu1*	
Sipa1l1	*Psmg4*	*Msh3*	
Sirpa	*Rbm4b*	*Mtx3*	
Slc38a6	*Rps6ka1*	*Mycbp2*	
Slc4a7	*Ryr2*	*Myo5a*	
Tank	*Sipa1l1*	*N4bp2l1*	

Tk1	*Slc38a6*	*Nadk*
Tlr4	*Slc41a3*	*Nsmce1*
Tmem147os	*Slc4a7*	*Ntpcr*
Ttc17	*Srgap2*	*P2ry14*
Ttn	*Stag2*	*Pfkfb1*
Vdac3	*Tank*	*Phldb1*
	Tpd52	*Pitpnc1*
	Ttc17	*Pnpla6*
	Ttn	*Ppcdc*
	Zdhhc3	*Prkacb*
		Psmg4
		Rai14
		Rbm4b
		Rcbtb2
		Rps6ka1
		Ryr2
		Sipa1l1
		Sirpa
		Slc38a6
		Slc41a3
		Slc4a7
		Srgap2
		Stag2
		Tank
		Tk1
		Tlr4
		Tmem147os
		Tpd52
		Ttc17
		Ttn
		Vdac3
		Zdhhc3

Table S9. Differentially spliced exon clusters

Gene	spliced region	p.adjust	comparison
Ank3	chr10:70004991:70015568:clu:3992:+	<0.0001	KO.PBS-vs-KO.ASO
Ank3	chr10:70004991:70015568:clu:6143:+	<0.0001	WT.PBS-vs-WT.ASO
Ttn	chr2:76852137:76857904:clu:3807:-	<0.0001	WT.PBS-vs-WT.ASO
Ttn	chr2:76800580:76803293:clu:9340:-	<0.0001	KO.PBS-vs-KO.ASO
Msh3	chr13:92349337:92353225:clu:1249:-	<0.0001	KO.PBS-vs-KO.ASO
	chr8:40124967:40128477:clu:1877:+	<0.0001	KO.PBS-vs-KO.ASO
	chr8:40124967:40145292:clu:1877:+	<0.0001	KO.PBS-vs-KO.ASO
Ttn	chr2:76800580:76803293:clu:3801:-	<0.0001	WT.PBS-vs-WT.ASO
Cadm1	chr9:47810143:47813773:clu:8920:+	<0.0001	KO.PBS-vs-KO.ASO
Ttn	chr2:76857987:76859460:clu:9346:-	<0.0001	KO.PBS-vs-KO.ASO
	chr8:40124967:40128477:clu:1612:+	<0.0001	WT.PBS-vs-WT.ASO
	chr8:40124967:40145292:clu:1612:+	<0.0001	WT.PBS-vs-WT.ASO
Ldb3	chr14:34573012:34578595:clu:2330:-	<0.0001	WT.PBS-vs-WT.ASO
Ldb3	chr14:34577344:34578595:clu:2330:-	<0.0001	WT.PBS-vs-WT.ASO
Ttn	chr2:76818816:76821116:clu:9341:-	<0.0001	KO.PBS-vs-KO.ASO
Gcnt1	chr19:17333256:17356557:clu:2489:-	0.001	KO.PBS-vs-KO.ASO
Tk1	chr11:117817191:117818999:clu:5749:-	0.002	WT.PBS-vs-WT.ASO
Tk1	chr11:117817191:117822097:clu:5749:-	0.002	WT.PBS-vs-WT.ASO
Evl	chr12:108555213:108648315:clu:8998:+	0.002	WT.PBS-vs-WT.ASO
Evl	chr12:108635884:108648315:clu:8998:+	0.002	WT.PBS-vs-WT.ASO

	chr10:111610773:111610995:clu:6227:+	0.003	WT.PBS-vs-WT.ASO
Nadk	chr4:155562455:155576993:clu:4393:+	0.003	KO.PBS-vs-KO.ASO
Nadk	chr4:155563979:155576993:clu:4393:+	0.003	KO.PBS-vs-KO.ASO
P2ry14	chr3:59116291:59130494:clu:7401:-	0.003	WT.PBS-vs-WT.ASO
P2ry14	chr3:59116291:59153419:clu:7401:-	0.003	WT.PBS-vs-WT.ASO
Ntpcr	chr8:125733231:125736068:clu:2069:+	0.005	KO.PBS-vs-KO.ASO
Ntpcr	chr8:125734349:125736068:clu:2069:+	0.005	KO.PBS-vs-KO.ASO
Pnpla6	chr8:3537883:3541291:clu:1822:+	0.006	KO.PBS-vs-KO.ASO
Pnpla6	chr8:3538085:3541291:clu:1822:+	0.006	KO.PBS-vs-KO.ASO
Fhod1	chr8:105334802:105336382:clu:5762:-	0.015	KO.PBS-vs-KO.ASO
Fhod1	chr8:105336260:105336382:clu:5762:-	0.015	KO.PBS-vs-KO.ASO
Dusp16	chr6:134761434:134791238:clu:1182:-	0.017	WT.PBS-vs-WT.ASO
Dusp16	chr6:134761434:134792277:clu:1182:-	0.017	WT.PBS-vs-WT.ASO
Ttc7	chr17:87308844:87321403:clu:3055:+	0.018	KO.PBS-vs-KO.ASO
Ttc7	chr17:87309712:87321403:clu:3055:+	0.018	KO.PBS-vs-KO.ASO
Ttn	chr2:76818816:76821116:clu:3802:-	0.024	WT.PBS-vs-WT.ASO
spliced EST	chr13:67876641:68213614:clu:1206:-	0.025	KO.PBS-vs-KO.ASO
spliced EST	chr13:68213543:68213614:clu:1206:-	0.025	KO.PBS-vs-KO.ASO
Evl	chr12:108555213:108648315:clu:2780:+	0.028	KO.PBS-vs-KO.ASO
Evl	chr12:108635884:108648315:clu:2780:+	0.028	KO.PBS-vs-KO.ASO

Table S10. Genes reverted by ASO treatment

GOterm – biological process	Associated genes
lymphocyte homeostasis	*Ahr, Casp3, Cd24a, Cd44, Cd74, Coro1a, Dock10, Dock11, Gpam, Lyn, Nckap1l, P2rx7, Pik3cd, Pirb, Ripk3, Slc40a1, Tnfsf13b*
immune effector process	*Ace, Aim2, Angpt1, Anxa3, Apbb1ip, Apobec1, Arrb2, Atp7a, Bst2, C1qa, C1qb, C1qc, C1ra, C1s1, C3, C4b, Cadm1, Cd24a, Cd37, Cd74, Cd84, Cfh, Cfp, Clec2d, Coro1a, Ctsc, Ctsh, Cxcl9, Ddx58, Dock10, Dock11, Fam49b, Fcgr2b, Fcgr3, Fes, Fxyd1, Gbp2b, Gpam, H2-D1, H2-DMa, H2-K1, Ifih1, Ifit2, Ifitm1, Ifitm2, Ifitm3, Ighm, Il18, Il27ra, Il33, Inpp5d, Irak3, Irf7, Isg15, Itm2a, Kit, Lat2, Lbp, Lfng, Lyn, Lyst, Milr1, Mx2, Ncf1, Oas2, Oasl2, P2rx7, Pirb, Plcg2, Pnp, Prkcd, Prkce, Ptk2b, Ptpn6, Pycard, Rab27a, Rgcc, Ripk3, Rnasel, Rsad2, Rtp4, Sema4a, Serping1, Slc11a1, Stat2, Stxbp2, Swap70, Syk, Tlr7, Tmem173, Trim25, Trim30a, Tspan6, Tyrobp, Unc93b1, Vav1, Vsir, Was, Zc3hav1*
leukocyte mediated immunity	*Ace, Anxa3, Arrb2, Bst2, C1qa, C1qb, C1qc, C1ra, C1s1, C3, C4b, Cadm1, Cd24a, Cd74, Cd84, Clec2d, Coro1a, Ctsc, Ctsh, Fam49b, Fcgr2b, Fcgr3, Fes, H2-D1, H2-DMa, H2-K1, Ighm, Il18, Il27ra, Inpp5d, Irf7, Kit, Lat2, Lyn, Lyst, Milr1, Ncf1, P2rx7, Pirb, Pnp, Prkcd, Ptpn6, Rab27a, Ripk3, Rsad2, Serping1, Slc11a1, Stxbp2, Swap70, Syk, Vav1, Vsir, Was*
regulation of cell-substrate adhesion	*Cdk6, Clasp1, Col8a1, Coro1c, Dab2, Egflam, Fn1, Gpm6b, Hsd17b12, Iqgap1, Itga6, Mmp14, Myoc, Nid1, Ninj1, Pdpn, Plau, Postn, Prex1, Prkce, Ptk2b, Ptn, Ptprj, Rsu1, Sdc4, Spp1, Thy1*
positive regulation of cell-substrate adhesion	*Cdk6, Col8a1, Dab2, Egflam, Fn1, Hsd17b12, Iqgap1, Itga6, Myoc, Nid1, Ninj1, Prex1, Prkce, Ptk2b, Ptn, Ptprj, Rsu1, Sdc4, Spp1, Thy1*
antigen processing and presentation	*Cd74, Fcgr2b, Fcgr3, H2-Aa, H2-D1, H2-DMa, H2-DMb1, H2-Eb1, H2-K1, H2-Q7, Ifi30, Ighm, Psmb8, Psmb9, Pycard, Rab27a, Rab32, Rab8b, Slc11a1, Tap1, Unc93b1, Was*
antigen processing and presentation of peptide antigen	*Cd74, Fcgr2b, Fcgr3, H2-Aa, H2-D1, H2-DMa, H2-DMb1, H2-Eb1, H2-K1, H2-Q7, Ifi30, Pycard, Slc11a1, Tap1, Unc93b1*
response to virus	*Aim2, Apobec1, Bst2, Cd37, Cdk6, Cfl1, Cxcl9, Ddx58, Fxyd1, Gbp2b, Gpam, Hspb1, Ifi27l2a, Ifih1, Ifit2, Ifitm1, Ifitm2, Ifitm3, Il33, Irak3, Irf7, Isg15, Lcn2, Lgals9, Lyst, Mx2, Npc2, Oas2, Oasl2, Pycard, Rnasel, Rsad2, Rtp4, Stat2, Tlr7, Tmem173, Trim25, Trim30a, Tspan6, Unc93b1, Zc3hav1*

defense response to virus	*Aim2, Apobec1, Bst2, Cd37, Cxcl9, Ddx58, Fxyd1, Gbp2b, Gpam, Ifih1, Ifit2, Ifitm1, Ifitm2, Ifitm3, Il33, Irf7, Isg15, Lyst, Mx2, Oas2, Oasl2, Pycard, Rnasel, Rsad2, Rtp4, Stat2, Tlr7, Tmem173, Trim25, Trim30a, Tspan6, Unc93b1, Zc3hav1*

Table S11: Gene list for WikiPathway analysis

GOterm – WikiPathway	Associated genes
Oxidative phosphorylation	*Atp5d, Atp5e, Atp5g1, Atp5g2, Atp6ap2, Ndufa11, Ndufa2, Ndufa3, Ndufa7, Ndufb7, Ndufs2, Ndufs7, Ndufs8, Ndufv1, Ndufv3*
Fatty Acid Beta Oxidation	*Acadl, Acads, Acadvl, Acat1, Acsl4, Acsl5, Cpt1b, Crat, Decr1, Eci1, Hadh, Hadha, Pnpla2, Slc25a20, Tpi1*
IL-5 Signaling Pathway	*Alox5ap, Btk, Csf2rb, Hck, Hcls1, Itgam, Itgb2, Jun, Lyn, Map2k2, Pik3cg, Pla2g4a, Prkcb, Prkcd, Ptk2b, Ptpn6, Rps6ka1, Sdcbp, Shc2, Syk, Vav1*
Chemokine signaling pathway	*Adcy5, Adcy6, Adcy7, Adcy9, Arrb1, Arrb2, Ccl11, Ccl2, Ccl5, Ccl6, Ccl7, Ccl8, Ccr1, Ccr2, Ccr5, Cxcl1, Cxcl13, Cxcl16, Cxcl2, Cxcl5, Cxcr4, Dock2, Elmo1, Fgr, Gnai3, Gnb3, Gng11, Gng2, Hck, Lyn, Ncf1, Pak1, Pik3cd, Pik3cg, Pik3r5, Plcb2, Prex1, Prkcb, Prkcd, Ptk2b, Rac2, Rap1b, Shc2, Vav1, Was*
Spinal Cord Injury	*Anxa1, Btg2, Casp3, Ccl2, Ccnd1, Ccr2, Cd47, Cdk1, Cxcl1, Cxcl2, Egr1, Epha4, Fcgr2b, Il1b, Il1r1, Il6, Mbp, Mmp12, Myc, Nox4, Nr4a1, Ntn1, Pirb, Rtn4, Tlr4, Tnfsf13b, Vim, Zfp36*
TYROBP Causal Network	*Abcc4, Apbb1ip, Bin2, C1qc, C3, Capg, Cd37, Cd84, Cxcl16, Cytl1, Elf4, Gpx1, Hcls1, Igsf6, Il10ra, Il18, Itgam, Itgax, Itgb2, Kcne3, Lhfpl2, Maf, Ncf2, Nckap1l, Npc2, Nrros, Plek, Ppp1r18, Pycard, Rgs1, Rps6ka1, Samsn1, Spp1, Tcirg1, Tgfbr1, Tmem106a, Tnfrsf1b, Tyrobp, Zfp36l2*
Microglia Pathogen Phagocytosis Pathway	*C1qa, C1qb, C1qc, Cybb, Fcer1g, Fcgr1, Hck, Itgam, Itgb2, Lyn, Ncf1, Ncf2, Ncf4, Nckap1l, Pik3cd, Pik3cg, Plcg2, Ptpn6, Rac2, Siglece, Syk, Trem2, Tyrobp, Vav1*
Complement and Coagulation Cascades	*C1qa, C1qb, C1qc, C1ra, C1s1, C3, C3ar1, C4b, C7, Cd55, Cfb, Plat, Plau, Pros1, Serpine1, Serping1, Vwf*

Table S12. Primers for splice PCR

Primer	Sequence
mCamk2d_ex12_f	GGCGCCATCTTGACAACTATG
mCamk2d_ex16_r	CTTTCACGTCTTCATCCTCAATGG
mTtnPEVK_ex4_f	CCTACTCCCATGATTCCAGCAAAAGCTTC
mTtnPEVK_ex13_r	CTTTAGCTGGAGGGGCTTCC
mLdb3_iso_fw	CCTATTCCCATCTCCACGAC
mLdb3_iso_rev	GAGACTGCAGGTTGGAGGAC
mAnk3_E22_f	CATCACGGAGAAGCACAAAA
mAnk3_E25_r	GGCTCCAAGACTGAAGCCTA
hLDB3_E3_fwd	CCTCACTATCTCCCGGATCA
hLDB3_E6_rev	AATTCTGTCCCCGTCATCTG
hCAMK2D_E12_fwd	AAGGGTGCCATCTTGACAAC
hCAMK2D_E16_rev	TGCTTTCGTGCTTTCACATC

Table S13. Primers and probes for quantitative real-time PCR (RT-qPCR)

Primer and probe	Sequence
mBnp-fwd	AGCTGCTGGAGCTGATAAGAGAA
mBnp-rev	GTGAGGCCTTGGTCCTTCAA
mBnp-probe	6-FAM-AGTCAGAGGAAATGGCCCAGAGACAGCTA-TAMRA
mRbm20-fwd	CTGGGAACCGGAGGTGTT
mRbm20-rev	GTCCTGGGAACCACGAACT
mRbm20-probe	CCACTCCTAGAGGAATGC
mRbm20-fwd	CAAGAAGGAGCTGACGACAAA
mRbm20-rev	TCTGTCCCTTCCTGCTGTAT
mRbm20-probe	AATGAGGCTGGAGCTGAGGAACAG
hRBM20-fwd	TGAGCTGAACGACTTTCACG
hRBM20-rev	TGCAGCTTCCCTTTCACAT
hRBM20-probe	CCTCCACTTGCCGCATATCTGTAGC

For: forward; rev: reverse; 6-FAM: 6-carboxyfluorescein; TAMRA: 6-carboxytetramethylrhodamine.

Table S14. Amplicons for quantitative real-time PCR (RT-qPCR)

Set	organism	Order number	Manufacturer
Eef1a1	mouse	Mm01973893-g1	Applied Biosystems
Nppa	mouse	Mm01255747-g1	Applied Biosystems
Fhl1	mouse	Mm04204611-g1	Applied Biosystems
Fhl2	mouse	Mm00515781-m1	Applied Biosystems
ACTN2	human	Hs00153809-m1	Applied Biosystems
RBM20	human	Hs01098240-m1	Applied Biosystems

Table S15. Antibodies for Western blot.

Antibody	Species	Dilution	Manufacturer	ID
RBM20	rabbit	1:100	Own production	-
RBM20	rabbit	1:10	Abcam	ab233147
CAMK2D	rabbit	1:200	Abcam	ab181052
FHL1	mouse	1:500	Sigma-Aldrich	WH0002273M1
FHL2	mouse	1:100	MBL	K0055-3
Tubulin	mouse	1:500	Sigma-Aldrich	T6557

Table S16. Antibodies for immunofluorescence staining

Antibody	Species	Dilution	Manufacturer	ID
RBM20	rabbit	1:50	Atlas	HPA035806
α-Actinin EA53	mouse	1:200	Sigma	A7811
α-Actinin EA53	mouse	1:200	Abcam	Ab9465
Alexa Fluor 488	goat	1:1000	Thermo Fisher	A11034
Alexa Fluor 568	goat	1:1000	Thermo Fisher	A11031